nature geoscience

SUPPLEMENTARY INFORMATION

https://doi.org/10.1038/s41561-019-0345-3

In the format provided by the authors and unedited.

Lunar soil hydration constrained by exospheric water liberated by meteoroid impacts

M. Benna [1,2]*, D. M. Hurley [3], T. J. Stubbs [1], P. R. Mahaffy [1] and R. C. Elphic [4]

---

[1]NASA Goddard Space Flight Center, Greenbelt, MD, USA. [2]CSST, University of Maryland, Baltimore County, Baltimore, MD, USA. [3]The Johns Hopkins University Applied Physics Laboratory, Laurel, MD, USA. [4]NASA Ames Research Center, Moffett Field, CA, USA. *e-mail: mehdi.benna@nasa.gov

Supplementary Information for

Lunar Soil Hydration Constrained by Exospheric Water Liberated by Meteoroid Impacts

M. Benna, D. M. Hurley, T. J. Stubbs, P. R. Mahaffy, and R. C. Elphic

Correspondence to: mehdi.benna@nasa.gov

This PDF file includes:

Supplementary Materials S1 to S6
Supplementary Figures 1 to 17
Supplementary Tables 1 to 2

S1. Details of the NMS Observations of Exospheric Water and Data Reduction:

Over the course of the LADEE mission, the NMS instrument was operated intermittently at a rate that ranged from 5 operations per day, early in the mission, to ~ 20 operations per day in the month leading up to the spacecraft impacting the surface of the Moon. The vast majority of these NMS activities were dedicated to measuring volatile species (including water) in the exosphere of the Moon. The typical NMS activity lasted 30 – 60 min, during which the instrument scanned through a series of predefined mass-per-charge channels corresponding to the volatile species of interest. Water abundance was tracked at the mass-per-charge channel m/z = 18. The instrument's periods of activity were interleaved by periods of inactivity of varying extents (median duration of 129 min), during which the sensor remained cold. Supplementary Fig. 5 provides a temporal distribution of the activities that were dedicated to measuring exospheric water over the course of LADEE's science phase.

When measuring the composition and densities of neutrals, the NMS sensor utilizes electron impact ionization to convert the incoming exospheric neutral gas into an ionized stream that can be measured by the analyzer. Electron impact ionization is produced by an electron beam emitted from a hot filament. When the filament is on, its temperature can reach an excess of 2700 °C. The heat dissipated by the hot filament propagates progressively by conductive and radiative transfer from the ion source region to the adjacent sensor's elements. As these elements warm up, they outgas several adsorbed species (water being one), which in return raise the background pressure in the sensor. In the case of water, the increase of this thermally induced outgassing manifests itself as a rise in the raw count rate of the water channel from a typical few counts/s in the first few minutes after filament turn-on to ~ 300 – 1000 counts/s by the end of the activity. Supplementary Fig. 6 provides an example of a typical signal profile of water $s_i(t)$ that was collected during the NMS activity i of interest, and shows the typical signature of thermally induced background.

The amplitude of the water signal at the exact time of the filament turn-on (t = 0 s) is not directly accessible. This is because the first two minutes of each activity are dedicated to the ramp-up of filament emission and the collection of noise measurements on the detector. The instrument did not begin to sample the water mass channel until ~120 s had elapsed from the time the filament was initially biased. To reconstruct the amplitude of the water signal $s_{i,on} = s_i(0)$ at t = 0 s, the measurements collected from t = 120 s to 420 s are extrapolated in time using an outgassing template profile $s(t)$. For any given activity i, the rise of water signal with time follows a scaled version of this outgassing template profile. The outgassing template is a representative time profile constructed by fitting the median amplitudes of water signal collected at $120\ s \leq t\ \leq 420\ s$ from all activities, and binned in 20 s bins. The median amplitudes are fitted with a second-order polynomial $p(t) = p_0 + p_1 t + p_2 t^2$, where $p_0 = 1.537 \pm 0.412$, $p_1 = 1.615 \times 10^{-1} \pm 6.1 \times 10^{-3}$, and $p_2 = 2.193 \times 10^{-4} \pm 0.128 \times 10^{-4}$. A second-order fit was chosen because the outgassing rate grows linearly in time with the heated surface area, and so does the derivative of the gas density (see Eq. 12). The resulting outgassing template is shown in Supplementary Fig. 7. For a given activity i, the amplitude of the water at turn on $s_{i,on}$ is derived by solving the least-squares minimization: $\left\| s_i(t) - \frac{s_{i,on}}{p} p(t) \right\|^2$.

During the period of inactivity, the temperature of the sensor's walls fluctuated by several tens of degrees as the spacecraft orbited the Moon and cycled through various attitudes. This temperature variation altered the adsorption/desorption balance inside the sensor and, consequently, changed the water density that would be measured at the time of instrument turn-on. To mitigate the effect of temperature variation, a corrected signal level $c_{i,on}$ is calculated from the raw measurement $s_{i,on}$ collected at a sensor temperature $T_{i,on}$ by applying a temperature correction function $R_T(T)$. The corrected signal level $c_{i,on}$ is given by:

$$c_{i,on} = \frac{s_{i,on}}{R_T(T_{i,on})} \tag{2}$$

The temperature correction function is derived by examining the temperature dependence of the measured signals $\left[\ s_{i,on}\right]_{i=all\ activities}$. As Supplementary Fig. 8 shows, the measurements are distributed over a temperature that ranges from 5 °C to 105 °C. The amplitude of each measurement represents the cumulative effects of the contribution of ingested exospheric water (the useful signal, in our case) and of the intrinsic instrument outgassing background (i.e., background produced by the natural outgassing of the sensor in the absence of any contribution of the exosphere). With 743 distinct measurements, one can safely assume that, for a given sensor temperature, the lowest recorded signal was achieved when the exospheric water contribution was at its lowest (or null), and where the instrument's intrinsic background was at its steady-state minimum. The variation of signal level across these minima is solely the result of sensor temperature variation. The temperature correction function is then derived by fitting these minima data points. The resulting function is:

$$R_T(T_{i,on}) = 19.0 \exp\left(\frac{T_{i,on} - 87.5}{9.5}\right) + 1 \tag{3}$$

This function makes a correction of only 5% for data collected at 40 °C, but rescales them by a factor 16 when they are collected at 80 °C.

As will be described in the next section, the measured signal is the result of the combined contributions of instrument background generated by the interaction of exospheric water with the sensor walls, and of the background produced by the natural outgassing of the sensor (with no external burden). This intrinsic outgassing is generated by remote areas of the sensor (including the getter) that are very loosely coupled with the ion source region. The level of this intrinsic background fell below the instrument detection limit by the end of Dec. 2014 (one month into the LADEE science phase), and we elect to subtract its effect from the early mission data. As in the case of the temperature correction, the intrinsic background of the sensor was obtained by fitting the minima measurements that were collected from 7 Nov 2014 to 25 Dec 2014 by an exponential decay function:

$$c_b(t) = 4.5\,\exp(-\frac{t - 1.44 \times 10^5}{1.65 \times 10^5}) \tag{4}$$

where t is the elapsed time (in seconds) since the beginning of the science phase of the mission. The density $n_{i,on}$ of the water inside the sensor at the time of filament turn-on $t_{i,on}$ of activity *i* can then be reconstructed by applying all the aforementioned corrections:

$$n_{i,on} = \frac{1}{S_{H_2O}}\left[\frac{s_{i,on}}{R_T(T_{i,on})} - c_b(t_{i,on})\right] \tag{5}$$

$S_{H_2O} = 0.025 \pm 0.002\ (counts/s)/(molecules/cm^3)$ is the instrument sensitivity to water, which was calculated from the normalized instrument sensitivity[21] assuming a water ionization cross section $\sigma = 2.275\ \text{Å}^2$ at 70 eV. Supplementary Fig. 9 summarizes the different steps of data reduction when applied to the full set of water measurements.

Uncertainties in the reduced data are due to the combination of random errors and systematic errors. Random errors follow a Poisson distribution and are mainly due to counting statistics. They were propagated through the steps of the data-reduction scheme, and their σs are typically less than 15% of the reduced values. Systematic errors are mainly due to the extrapolation using the outgassing template profile. They are also propagated through the data-reduction scheme, and they lead to a near normal distribution with σ at 30%. Random errors play a role in the uncertainty of the derived thickness of the desiccated layer, and systematic errors dictate the uncertainty of the derived water loss flux rates and hydration levels of the underlying soil.

As depicted in Supplementary Fig. 2, one important characteristic of the reduced data is the lack of correlation with the duration of instrument inactivity. We will show in the next section (Eq. 22), that strong correlation would only occur if the densities of water in the exosphere were near constant.

S2. Analytical Formulation of NMS Interaction with Exospheric Water:

The NMS instrument was exposed to lunar exospheric water through a set of two apertures and a series of ram-facing vents. Exospheric water enters the sensor through these orifices at a velocity $\overrightarrow{v_e} = \overrightarrow{v_{ex}} + \overrightarrow{v_{sc}}$, where $\overrightarrow{v_{ex}}$ and $\overrightarrow{v_{sc}}$ are the exospheric flow velocity and the spacecraft orbital velocity, respectively, measured in an inertial frame. Once inside the sensor, ingested water molecules undergo a series of collisions with the internal walls. Following each collision, water molecules can thermally accommodate with the temperature of the surface before being reemitted to the gas phase. They can also physisorb for a duration controlled by the rate of desorption. Some of the physisorbed molecules may further chemisorb to an irreversible state. Physisorbed molecules can also desorb and return to the gas phase. The rates of adsorption and desorption vary with many physical parameters, chief among which are the surface properties and temperature. Eventually, after multiple surface interactions (reflection or adsorption/desorption cycles), some of the water molecules will find their way out of the sensor through one of the orifices. At any given time, the density inside the sensor results from a balance between the influx of water molecules into the sensor, surface adsorption, and surface desorption, and venting of molecules to space. Additional details on instrument geometry and internal design are provided by Mahaffy *et al.*[21] and in the NMS PDS Software Interface Specification[47]. The NMS instrument measures gas density in the ion source region (also referred to in the paper as" the ion source" or "the source"). This region interacts with the lunar environment through one of the apertures aforementioned. It also exchanges with the rest of the sensor volume through a conductance-limited path. As such, the ion source region and the rest of the sensor (including the getter) are very weakly coupled. As discussed in the preceding section, the effect of the rest of the sensor on the density in the ion source region is only noticeable in the first two months of the science phase as the intrinsic background of Eq. 4. Since this background was subtracted from the data, we can assume that the entire sensor is reduced to its ion source region.

Using the Langmuir adsorption model[48], the net rate of change of water density that is measured in the ion source region can be expressed as:

$$V_s \frac{dn_s}{dt} = F_i - F_o + F_d - F_a \tag{6}$$

where n_s is the density of the water in the ion source region, and V_s is its internal volume. F_i is the flux of water molecules entering through the source aperture. F_o is the flux of molecules exiting the source region to space. F_a is the flux of molecules adsorbing on the internal surfaces. F_d is the flux of molecules desorbing out of the walls and back to the gas phase.

The flux of water molecules entering through the aperture is[49]:

$$F_i = n_e A_o \sqrt{\frac{kT_e}{2\pi m}} \left[\exp(-S^2) + S\sqrt{\pi}(1 + \operatorname{erf}(S))\right] = n_e A_o \sqrt{\frac{kT_e}{2\pi m}}\, F(S) \tag{7}$$

where n_e is the density of the water in the exosphere, T_e is the exospheric gas temperature, *m* is the molecular mass of water, *k* is the Boltzmann constant, and A_o is the area of the source aperture. $F(S)$ is the ram enhancement factor. S is the speed ratio given by:

$$S = v_e \sqrt{\frac{m}{2kT_e}} \cos(\theta) \tag{8}$$

θ being the flow incidence angle (angle between $\overrightarrow{v_e}$ and the normal to the aperture plane).

The flux exiting the ion source region can be expressed as:

$$F_o = n_s A_o \sqrt{\frac{kT_s}{2\pi m}} \tag{9}$$

where T_s is the average temperature of the source walls.

The flux of molecules adsorbing from the gas phase onto the ion source walls due to the density contribution can be written as:

$$F_a = n_s A_s \sqrt{\frac{kT_s}{2\pi m}} (1 - \theta_s)\alpha \tag{10}$$

where A_s is the area of the source region that is available for adsorption. θ_s is the fraction of the area A_s which is covered by physically adsorbed molecules due to the exposure to the density n_s. α is the sticking coefficient of water on the source surfaces at temperature T_s.

Finally, the flux of molecules desorbing from the source walls due to adsorbed molecules with the surface coverage θ_s can be written as:

$$F_d = A_s \nu \theta_s \tag{11}$$

where ν is the number of molecules that desorbs per second from a unit area that is coated with one monolayer of adsorbates.

The net change of densities n_s inside the source region is then:

$$V_s \frac{dn_s}{dt} = n_e A_o \sqrt{\frac{kT_e}{2\pi m}}\, F(S) + A_s \nu \theta_s - n_s \sqrt{\frac{kT_s}{2\pi m}}\, [A_o + A_s(1 - \theta_s)\alpha] \tag{12}$$

Additionally, the rate at which the surface coverage θ_s changes can be expressed as:

$$\frac{d\theta_s}{dt} = \frac{F_a - F_d}{A_s Z} = \frac{n_s \sqrt{\frac{kT_s}{2\pi m}} (1 - \theta_s)\alpha - \nu\theta_s}{Z} \tag{13}$$

where Z is the number of molecules that would form a monolayer on one unit area.

To further simplify Eq. 12, we can assume that the ion source region is continuously at or near steady state ($\frac{dn_s}{dt} \approx 0$). This would be the case if the source's outgassing time constant τ is large. As we will show in the next section, this time constant is indeed large ($\tau = 1690\ s$) compared to the time scale of fluctuations in the exosphere. Additionally, prior to launch, the NMS sensor was baked to 250 °C under ultra-high vacuum for multiple days. It then remained sealed until it reached the lunar orbit (with the getter pumping irreversibly any residual water). It is then safe to assume that at the start of the science phase of the mission, the surface coverage of physically adsorbed water was negligible $\theta_s \ll 1$. n_s can then be derived from Eq. 12 as:

$$n_s = \frac{\sqrt{\frac{2\pi m}{kT_s}}}{[A_o + A_s\alpha]}\left[n_e A_o \sqrt{\frac{kT_e}{2\pi m}}\, F(S) + A_s \nu \theta_s\right] \tag{14}$$

which can be injected in Eq. 13 to get:

$$\frac{d\theta_s}{dt} = \frac{A_o \nu}{Z[A_o + A_s\alpha]}\left[n_e \frac{\alpha}{\nu}\sqrt{\frac{kT_e}{2\pi m}}\, F(S) - \theta_s\right] \tag{15}$$

The term $\frac{Z[A_o+A_s\alpha]}{A_o\nu}$ has a dimension of time and will be labeled τ. We will show in section S3 that $\tau = 1690\ s$. Eq. 15 can then simply be written as a first-order linear constant coefficient differential equation with a forcing term:

$$\frac{d\theta_s}{dt} + \frac{\theta_s}{\tau} = n_e \frac{\alpha}{\tau\nu}\sqrt{\frac{kT_e}{2\pi m}}\, F(S) \tag{16}$$

Note that, while omitted, θ_s, n_e, and S are all functions of time.

The solution to this differential equation at an arbitrary time $t_1$is:

$$\theta_s(t_1) = \frac{\alpha}{\tau\nu}\sqrt{\frac{kT_e}{2\pi m}} \int_{t_0}^{t_1} n_e(x)\, F(S(x)) e^{-\frac{t_1 - x}{\tau}} dx + \theta_s(t_0) e^{-\frac{t_1}{\tau}} \tag{17}$$

Since, in most cases, the duration of inactivity of the instrument $t_{on} - t_{off} > 4\tau$, and $t_{on} \gg \tau$, Eq. 17 can be written for $t_1 = t_{on}$, and $t_0 = t_{off}$ as:

$$\theta_s(t_{on}) = \frac{\alpha}{\tau\nu}\sqrt{\frac{kT_e}{2\pi m}} \int_{t_{off}}^{t_{on}} n_e(x)\, F(S(x)) e^{-\frac{t_{on} - x}{\tau}} dx \tag{18}$$

The water density $n_s(t_{on})$ that would be measured at the start of any given activity can be derived by injecting Eq. 18 into Eq. 14 and using t as the integral variable.

$$\begin{aligned} n_s(t_{on}) = \sqrt{\frac{T_e}{T_s}}\Bigg[&\frac{A_o}{[A_o + A_s\alpha]} n_e(t_{on})\, F(S(t_{on})) \\ &+ \frac{A_s\alpha}{[A_o + A_s\alpha]}\frac{1}{\tau}\int_{t_{off}}^{t_{on}} n_e(t)\, F(S(t)) e^{-\frac{t_{on} - t}{\tau}} dt\Bigg] \end{aligned} \tag{19}$$

This equation is the full form of Eq. 1. It demonstrates that the measured water density at each instrument turn-on is a balance between the current density of the exosphere that is being subjected to the instrument and the integrated exospheric density ingested by the instrument during the period of inactivity. The integral term can be considered as the "memory" of the ion source region. The memory depth is captured by the time constant τ. The balance between "present" state (first term in the brackets) and "memory" (second term in the brackets) is set by the ratio $\frac{A_o}{A_s\alpha}$. In the extreme case of a non-active gas, such as Ar, that does not adsorb on sensor's walls ($\alpha \approx 0$), Eq. 19 reduces to the classical ram-enhancement equation[21]:

$$n_s(t_{on}) = \sqrt{\frac{T_e}{T_s}} n_e(t_{on})\, F(S(t_{on})) \tag{20}$$

One should also note that all properties of the sensor are captured by the two intrinsic constants $\frac{A_o}{A_s\alpha}$ and τ, and that no additional information on instrument design or behavior is needed. These two constants will be derived in the following section.

Since the average exospheric flow velocity $\overline{\overrightarrow{v_{ex}}}$ is statistically zero (flows can originate from all possible directions), the average value $\overline{E}$ of the term $\sqrt{\frac{T_e}{T_s}}F(S)$:

$$\overline{E} = \left[\overline{\sqrt{\frac{T_e}{T_s}}F(S)}\right] \cong \sqrt{\pi}\left[\overline{S\sqrt{\frac{T_e}{T_s}}}\right] \cong \sqrt{\pi}\,\overline{v_{sc}}\sqrt{\frac{m}{2k\overline{T_s}}} \tag{21}$$

which means that the exospheric temperature T_e has very little impact on the statistical distributions of the measured water densities (Eq. 19). With an average spacecraft speed $\overline{v_{sc}}$ = 1.7 km s^{-1}, and source temperature $\overline{T_s}$= 293 K, $\overline{E}$=10.3. For a large number of observations Eq. 19 can be replaced by the final form:

$$n_s(t_{on}) = \overline{E}\left[\frac{A_o}{[A_o + A_s\alpha]} n_e(t_{on}) + \frac{A_s\alpha}{[A_o + A_s\alpha]}\frac{1}{\tau}\int_{t_{off}}^{t_{on}} n_e(t)\, e^{-\frac{t_{on}-t}{\tau}} dt\right] \tag{22}$$

In this final equation, the measured water levels in the source are only dependent on the exospheric density and instrument intrinsic constants $\overline{E}$, $\frac{A_o}{A_s\alpha}$ and τ. The two latter will be derived in section S3.

If the water density in the lunar exosphere is constant, Eq. 19 further reduces to:

$$n_s(t_{on}) = \sqrt{\frac{T_e}{T_s}} n_e F(S)\left[1 - \frac{A_s\alpha}{[A_o + A_s\alpha]} e^{-\frac{t_{on}-t_{off}}{\tau}}\right] \tag{23}$$

This equation shows that in the case of a permanent and invariant exosphere, measured water densities at instrument turn-ons will be correlated with the duration of periods of inactivity ($t_{on} - t_{off}$). Furthermore, the distribution of measured water densities will replicate that of $e^{-\frac{t_{on}-t_{off}}{\tau}}$. Supplementary Fig. 10 depicts the cumulative distribution of the data as a function of the $\left[1-\frac{A_s\alpha}{[A_o+A_s\alpha]}e^{-\frac{t_{on}-t_{off}}{\tau}}\right]$ term. This profile is similar to the one derived for the case of a surface with no desiccated layer that is shown in Fig. 2B.

S3. Determination of the Source's Intrinsic Constants:

The outgassing time constant $\tau=\frac{Z[A_o+A_s\alpha]}{A_o\nu}$ of the ion source region can be derived by considering Eq. 14 in the absence of an outside exosphere (unburdened case):

$$A_s\nu\theta_s-n_s\sqrt{\frac{kT_s}{2\pi m}}\,[A_o+A_s(1-\theta_s)\alpha]=0 \tag{24}$$

One should notice that Eq. 24 is linear in n_s and θ_s, which allows us to write:

$$\frac{\theta_s}{n_s}\frac{dn_s}{dt}=\frac{d\theta_s}{dt} \tag{25}$$

Eq. 25 can be solved for $\frac{1}{n_s}\frac{dn_s}{dt}$ using Eq. 13 as:

$$\frac{1}{n_s}\frac{dn_s}{dt}=-\frac{A_o\nu}{Z[A_o+A_s\alpha]}=\frac{1}{\tau} \tag{26}$$

This equation shows that the instrument outgassing time constant τ can be derived directly from the unburdened decay profile of the recorded source density. Unfortunately, the NMS instrument was subjected continuously to the lunar exosphere. As such, its data does not provide the required information. To overcome this limitation, we used data from the Neutral Gas and Ion Mass Spectrometer (NGIMS)[50] that is currently orbiting Mars as part of the Mars Atmosphere and Volatile Evolution Mission (MAVEN).

The NGIMS instrument is nearly an identical instrument to NMS. The only difference between the two instruments resides in the fact that NGIMS ejects its getter as part of the break-off cap deployment at the beginning of the mission, while the NMS getter remains attached to the instrument for the duration of the mission. MAVEN orbits Mars along a 150 km × 6500 km elliptical orbit. The NGIMS instrument only operates while the spacecraft is below 500 km in altitude. The water measured by NGIMS is not from atmospheric origin. It is chemically synthesized inside the sensor by reaction of atmospheric atomic oxygen with hydrogen outgassed by the filament. When the spacecraft ascends to 500 km in altitude on the outbound portion of its orbit, the instrument is turned off. It remains inactive for the following ~3.5 h. It is turned on again when the spacecraft reaches 1500 km on the inbound portion of its orbit. While the instrument is inactive, the spacecraft is well above the atmosphere, and no water is being synthesized inside the sensor. The adsorbed water that was accumulated on the sensor's walls while the spacecraft was at a lower altitude is outgassed, unburdened by any atmospheric inputs. The outgassing time constant of the ion source region is captured in the profile of water decay while NGIMS is inactive and the spacecraft is at high altitude. Since NGIMS is identical in construction and material to NMS, the intrinsic time constant of NGIMS should reflect that of NMS. One should note that the water synthesis through recombination of atomic oxygen that takes place in the NGIMS source can only occur when the metal surfaces are near saturation (close to a monolayer of adsorbed atoms) during their exposure to the high densities of the oxygen-rich thermosphere of Mars. However, when the surface coverage is low, as in the case of NMS, the high reactivity of oxygen with the clean metal surface[51] (O is at least 1000 times more reactive than water) will lead to the atom irreversible chemisorption and sequestration in the metal lattice as an oxide, which will preclude its recombination as O_2 or H_2O. Hence, the water that was measured by NMS cannot be attributed to exospheric O.

In order to extract the time constant from the NGIMS data, we processed data from the first 4 days of the orbital phase of the MAVEN missions. During those first few days, the internal surfaces of the sensor were still pristine and should not have suffered the onset of oxidation due to the interaction with atomic oxygen from the atmosphere. The time constant of outgassing is determined from the water level $n_s(t_{off})$ prior to instrument turn-off and $n_s(t_{on})$ on the subsequent turn-on by:

$$\tau = \frac{t_{on} - t_{off}}{\log\left(\frac{n_s(t_{on})}{n_s(t_{off})}\right)} \tag{27}$$

Time constants for 18 successive periods of NGIMS inactivity are plotted in Supplementary Fig. 11, which yields a mean time constant $\tau = 1689\text{s} \pm 79\text{s}$.

The characteristic ratio $\frac{A_o}{A_s\alpha}$ is derived from data that were collected just prior to and after the break-off cap ejection. Prior to the break-off cap deployment, a measurement of water density was conducted. A simplified Eq. 14 provides the relation between the recorded density value n_b and surface coverage θ_b:

$$A_s v\theta_b = n_b\sqrt{\frac{kT_s}{2\pi m}}\, A_s\alpha \tag{28}$$

In the 360 seconds after the break-off deployment, another measurement was conducted. A second simplified Eq. 14 provides the relation between the recorded density value n_a and surface coverage θ_a:

$$A_s v\theta_a = n_a\sqrt{\frac{kT_s}{2\pi m}}\, [A_0 + A_s\alpha] \tag{29}$$

Since the outgassing time constant $\tau \gg 360$ s, one can safely assume that during the short period that separates the two set of measurements, the surface coverage remained nearly constant ($\theta_b = \theta_a$). The ratio $\frac{A_o}{A_s\alpha}$ can be derived by equating Eq. 28 and Eq. 29:

$$\frac{A_0}{A_s\alpha} = \frac{n_b - n_a}{n_b} \tag{30}$$

With $n_b = 1.71 \times 10^6 \pm 1.65 \times 10^4\ cm^{-3}$, and $n_a = 4.44 \times 10^5 \pm 8.42 \times 10^3\ cm^{-3}$, we derive $\frac{A_o}{A_s\alpha} = 2.86 \pm 0.06$.

S4. Modeling of Water Exopshere Dynamics and Correlation with NMS Observations:

In this study, we use the model described by Hurley and Benna[16] to simulate the evolution of released water produced by the impact of meteoroids on the surface of the Moon. This model simulates the dynamics of H_2O vapor released from meteoroids using a Monte Carlo numerical code that assigns an initial velocity to each particle and tracks them under lunar gravity assuming the gas is collisionless[52,53]. The numerical model propagates the particles using a 4th-order Runge-Kutta algorithm with 1 s time steps. The initial velocity of the vapor is assumed to be a Maxwell-Boltzmann distribution of a temperature T_e. Each of the initial 10^7 particles is randomly assigned a velocity magnitude taken from the distribution. The direction of the particles is isotropic in 2π steradians. At each time step, the particles are binned into a grid covering the volume of interest and recorded to provide the time evolution of the density. To resolve the progression of the vapor plume in the vicinity of the impact site, a special cube of 100 × 100 × 100 bins with a 1 km bin resolution is saved during the first 10 min of evolution. To examine the effects over the entire computational domain and over a longer evolution time, a spherical shell grid is used with grid cells of 0.25° angle × 10 km altitude that extend from the surface to 200 km in altitude. The state of these bins is tracked in 1 s time steps over 2 hours of real time. After 2 hours, the residual densities in the induced exosphere are negligible. Particles that reencounter the surface are assumed to adsorb on the surface and are removed from the simulation. The adsorption capacity of lunar regolith for water as a function of temperature is still a topic of debate[54,55,6,56,57]. For the purposes of this simulation, which is supposed to represent a generic impact applicable to any location on the Moon, we assume that the residence time of adsorbed particles is infinite. Although particles may continue to hop through the exosphere after encountering the surface, contribution to the overall density of impact vapor from particles on their second and subsequent hops is very low. Therefore, it is valid to neglect them. The code is run using 10^7 test particles. The collisionless assumption allows every particle to act independently. Therefore, the results can be scaled by any value as long as the collisionless assumption remains valid. For a 1 g water release, each test particle represents 3.3×10^{15} real particles. This scale factor is applied to convert model density into real density.

The impacting meteoroids that we consider have masses 10^{-12} g< m_i<10^6 g. The extrema of this range have been chosen based on practical considerations. Micrometeoroids with masses lower than 10^{-12} g make very little contribution to the total mass flux of the meteoroids complex[38]. Impactors larger than 10^6 g have an impact rate of 1 every 17 year, which is much longer than the duration of the LADEE mission. We assume that the impactors generate a water release that is $m_{w,i} = Y_{w,i} \times m_i$. $Y_{w,i}$ is the water yield for impactor i. Meteoroid impacts are generated randomly in time according to a preset rate distribution over a time span of 400 days. This time window is twice the duration of the LADEE mission, which allows us to account for the occurrence of low-probability, high-mass impactors. The impact location is drawn randomly on the surface assuming an isotropic meteoroid flux. The impactor velocity is also drawn randomly according to a probability distribution that was reconstructed based on the distribution of velocity of all the established meteoroids streams that encountered the Moon during NMS operational period (Supplementary Table 1). This velocity probability distribution is shown in Supplementary Fig. 12, has an average of 44.5 km s^{-1}, and is relatively symmetric.

An induced water exosphere is simulated for 2 hours after the impact using a Monte Carlo numerical code aforementioned. The densities in the induced exosphere (calculated for 1 g of water release) are then scaled by $m_{w,i}$ to reflect the contribution of an impactor of mass m_i. The scaled exosphere is convoluted by the spacecraft trajectory to produce an along-the-track density profile as would be observed by NMS. An integrated exosphere is constructed by superimposing the along-the-track densities generated by single impactors. The time span of the simulation is then truncated from 400 days to 197 days to reflect the exact duration of the LADEE science phase. Supplementary Fig. 13 provides an example of a randomly generated exosphere. Such an exosphere accounts for the contribution of more than 2×10^{15} individual impactors. A full mission scenario is simulated by calculating the water density that would be measured by NMS as reflected by Eq. 19 based on the actual LADEE observation timeline. For each study case, a series of 100 of these simulated missions was created, and a statistical average is produced from the resulting distributions of the NMS-simulated observations. It is these averaged distributions from several study cases that are discussed and compared in this study.

The flux model of impactors used in this study was chosen to follow a power law of mass $(m^{-\alpha(m)})$[58] where $\alpha(m)$ is derived from three main reference models that focused on a specific impactor mass range. These three reference models are referred to as the Grün's, the Halliday's, and the Brown's model. Grün *et al.*[34] compiled a reference impact flux distribution for meteoroid mass <1 g based on in situ experiments, zodiacal light observations, and oblique angle hypervelocity impact studies. More recently, the Grün's model was shown to be valid in the mass range 10^{-13} – 10^{-5} g using meteoroid flux density derived from the Hubble Space Telescope's solar arrays (data retrieved in 1993 and 2002)[59], and in the mass range 10^{-4} – 1 g using optical data from the Canary Island Long Baseline Observatory[60]. Brown *et al.*[36] has provided a flux distribution for impactors in the range of 1500 kg – 50,000 kg using satellite observations of optical flashes from bolides entering Earth's atmosphere. Finally, Halliday *et al.*[35] provided a flux model that covers the 0.1 – 12 kg range based on ground observation of 259 meteoritic fireballs by the Canadian Camera Network. The resulting combined flux model is shown in Fig. 2A.

The initial temperature T_e of the released water, while poorly constrained by past studies, can be bound by two extreme cases. The low-end temperature assumes that, when released, the shock-desorbed water is fully accommodated to the shocked regolith at the impact location. To be able to release water, the temperature of the shocked regolith has to be equal, at a minimum, to the temperature of complete physisorption and chemisorption of H_2O and OH molecules, which was measured to be ~ 500 K on Apollo lunar samples[45]. The high-end temperature assumes that desorbed molecules will further interact with the collision-dominated and hotter vapor plume that is generated by the impact. While Cintala *et al.*[43] recommend a temperature of ~ 4000 K, we used the more conservative higher temperature of 5000 K.

S5. Determination of Water Yield and Water Loss Rate Due to Impacts:

In all modeled cases, the water yield $Y_{w,i}$ is the only pertinent parameter that is adjusted in order to fit the distribution of the intensity of observed water events. For a given impactor i, the water yield $Y_{w,i}$ is prescribed by the volume $V_{d,i}$ of the target soil that is exposed to shock pressures above the water desorption threshold and the water concentration per weight H in the shocked regolith:

$$Y_{w,i} = \frac{\rho H V_{d,i}}{m_i} \tag{31}$$

where ρ is the density of the target regolith. The volume V_d can be estimated from shock pressure decay calculations, and H is used as the only free variable that can be tuned at will.

In a typical impact of a meteoroid on the porous lunar soil, the excavated material within the volume of the crater is subjected to peak shock pressures in excess of 500 GPa[38]. The amount of water desorbed by the impact shock-wave can be estimated by following an analogous treatment to that given by Morgan and Killen[61] for calculating vapor production rates. In the planar impact approximation[38], the peak pressure P_p in the target material due to an impactor of density ρ with an initial impact velocity v_i and mass m_i is given by:

$$p_p = \frac{\rho v_i^2}{4}\left[\frac{2C}{v_i} + S\right] \tag{32}$$

where C and S are empirical parameters of the target material relating shock-wave velocity u_s to particle velocity u_p. This approximation assumes that the mean densities ρ of the impactor and target, and their equations of states are the same. This peak pressure is corrected for the effects of target porosity n as:

$$p_p(d) = 1.2 p_p(1)[d + 0.05]^{3.6} \tag{33}$$

where the distention d is derived from the porosity n as:

$$d = \frac{1}{1 - n} \tag{34}$$

Values of C and S appropriate for various target materials are given in[62]. For regolith, ρ = 1800 kg m^{-3}, n = 0.4, C = 1.28, and S = 1.56.

The decay of peak pressure p with scaled distance $R = \frac{r}{r_i}$ from the impact center (r_i being the impactor radius) is given by:

$$\begin{cases} p(R) = p_p(d); for\ \ R < c \\ p(R) = p_p(d)[R - c]^{-\beta}; for\ \ R \geq c \end{cases} \tag{35}$$

c represents the scaled radius at the onset of the far field attenuation, and $\beta = (a v_i + b)$. This equation indicates that pressure decay in the near field is negligible and that the pressure attenuation in the far field is inversely proportional to a linear power law of impact velocity. The constants a, b, and c are derived from impact experiments. We adopt the values of 0.052 s km^{-1}, 1.19, and 2 for a, b, and c, respectively, as derived by Lange and Ahrens[63] from anorthosite onto anorthosite impacts.

Supplementary Fig. 14A provides examples of peak pressure decay curves for impact velocities of 5, 15 and 45 km s^{-1} as a function of radial distance from the impact center. These velocities were chosen to enable a direct comparison with the pressure profiles provided by Ahrens and O'Keefe[64] and reproduced by Melosh[38] for impact into anorthite. One should note that Eq. 35 generates the expected $r^{-3/2}$ decline of pressure in the far field region for low impact speeds, and r^{-3} for high impact speeds. As was noted by Melosh[38], the more rapid decline at high impact velocities is due to the fact that not all the energy behind the expanding shock is available to drive further expansion, since some of it is consumed in heating, melting, and vaporization of the material behind the shock front.

Incipient to complete water loss by shock devolatilization and melting occurs at impact pressures between 20 and 65 GPa[44], and total vaporization of the regolith will occur at the 236 GPa[43]. Total vaporization and loss of structural water occurs within a relatively close distance of the impact location, where the shock pressures are high. However, desorption of surface-adsorbed water occurs at lower pressure thresholds and takes place over a much more extended range and larger regolith volume. The activation energy E_d of desorption of water on lunar regolith samples and analogues was estimated to be 144 – 158 kJ mol^{-1}(45, 46). In this study, we adopt an average activation energy of 150 kJ mol^{-1}. The corresponding shock pressure required to desorb all water from the regolith is given by:

$$p_d = \frac{E_d \rho H}{0.018} = K_d H \tag{36}$$

where K_d is the desorption pressure for a cubic meter of water. The scaled radial distance R_d within which desorption would occur can then be derived as:

$$R_d = c + \left[\frac{p_p(d)}{p_d}\right]^{\frac{1}{\beta}} \tag{37}$$

Based on these equations, we calculate that water outgassing takes place to a radial distance $r_d = 57 r_i$ for the average impactor speed of 45 km s^{-1}. For comparison, it is about twice the typical radius of the resulting impact crater.

The volume V_c of the formed crater, its radius r_c, and its depth h_c are calculated using Eq. 18 and 20 of Holsapple[41] for impact into regolith targets. This volume is further scaled to encompass the shocked soils within the scaled radius R_d, and the resulting shocked volume is:

$$V_{d,i} = \left(\frac{R_d r_i}{r_c}\right)^3 V_c \tag{38}$$

In order to account for the presence of a desiccated top layer with a thickness h_t, the volume V_d is reduced by the volume occupied by the dry material. For large impactors, where the volume occupied by the dry top layer is negligible compared to the total volume of shocked regolith, the values of water yield converge asymptotically to:

$$Y_w = \frac{3H}{4\pi}\left(\frac{R_d}{r_c}\right)^3 V_c \tag{39}$$

One should note that the velocity-dependent pressure decay law of Eq. 35 generates a desorption volume scaling that is different from that of total volatilization. As illustrated in Supplementary Fig 14B, the pressure decay equation predicts the expected momentum-scaling of impacts in porous regolith (assuming a pressure threshold of total vaporization of 236 GPa[43]). This agrees with experimental and modeling studies[43,65-67]. These studies show that the volume of vaporized material, generated near the origin of the impact, increases with the impact velocity following a power law that range from v_i to v_i^2. It typically obeys an energy-scaling law ($\sim v_i^2$) in non-porous target material with a low coefficient of friction, and a momentum-scaling law ($\sim v_i$) in porous target material with a high coefficient of friction. However, due to the increase of the decline rate of the peak pressure in the far region with impact velocity, the volume of regolith shocked to desorption threshold (and thus the yield of desorbed water) decreases with the increase of impact velocity. This important fact explains why meteor streams with slow impact speeds yield exospheric water signatures that are larger than those of faster streams (See Methods: "Validity of the Intensities of the Observed Peak Events").

The best match between the distribution of observed events and those synthetically derived from the model is achieved by including a desiccated top layer that has a thickness of 8.0±1.0 cm (Fig. 2B). For the case of a water release temperature T_e = 500 K, a uniform hydration $H = 220$ ppm by weight is required below this desiccated layer in order to reflect the intensity of the observed events. The derived hydration is $H = 520$ ppm by weight for the case of temperature release T_e = 5000 K. The derived water yield as function of impactor mass is shown in Supplementary Fig. 15 for a target soil with a desiccated top layer of 8 cm. For impactors larger than 100 g, the contribution of the desiccated layer to the total mass of shocked regolith is negligible. The water yields for these large impactors converge asymptotically to 5.4 for T_e = 500 K, and 12.8 for T_e = 5000 K. Impactors with masses < 0.15 g don't pierce the dry layer and don't excavate hydrated soils. One should note that the derived water yield and the cut-off mass (0.15 g) are independent of the assumptions used in calculating the shocked volume V_d, its hydration level H, and the thickness h_t of the desiccated layer. As Eq. 31 shows, the water yield is dependent on the product $H \times V_d$. Consequently, when the model properly fits the data, an underestimation of V_d will result in a higher derived hydration H, and vice versa. The fact that this water concentration is in agreement with the average value (585 ppm) that was measured in the first top meter by LPND[18] provides a validation to our assumption that water outgassing takes place over the full volume subjected to shock pressures above the desorption threshold. Finally, one should note that desorption of water by the far-reaching shock wave involves volumes (and thus a water reservoir) that are 2 to 7 orders of magnitude larger than those mobilized by volatilization (Supplementary Fig. 14B). This large volume justifies the relatively large intensities of the detected NMS events despite the relatively low hydration of the soil.

The water loss rate $L_{w,i}$ of from the lunar surface due to meteoroids of mass m_i can simply be derived as:

$$L_{w,i} = Y_{w,i} F_i \tag{40}$$

where F_i is the mass flux on impacting meteoroids of mass m_i as subscribed by the Grün-Halliday-Brown model. Supplementary Fig. 16 provides the water loss rate as function of mass for the case of T_e = 500 K, and T_e = 5000 K, and shows that the total loss rate due to all meteoroid impacts is $1.3\times10^{-17} - 3.2\times10^{-17}$ g cm^2 s^{-1}.

S6. Identification of atypical events in the NMS data:

In order to correlate the events observed by the NMS with meteoroid streams, a metric of "Normalized Event Intensity Rate" $E_{w,\psi}(i)$ (NEIR) is calculated for each measurement i within a time window w and with a threshold signal level ψ:

$$E_{w,\psi}(i) = \frac{G_w(i) \times R_{w,\psi}(i)}{O_w(i)} \tag{41}$$

where $R_{w,\psi}$ is the number of observed events (Supplementary Fig. 1) within the time window w centered on observation i, and with intensities $> \psi$. $G_w(i)$ is the weighted average of measurements centered on observation i. O_w is the total number of NMS observations carried out in the same time period. We chose G_w to be a Gaussian weighted average of the NMS measurements with a full width half maximum of w. The use of a Gaussian function instead of a traditional boxcar function in the calculation of the moving average stems from the fact that the activity of most streams follows a shape that is closer to a Gaussian than to a rectangular profile[40]. To ensure that the averaging window contains at least one observation at any point in time, w was taken to be equal to 0.5 day based on the minimum observation rate of NMS of 2/day (as shown in Supplementary Fig. 5).

The threshold ψ is an adjustable parameter that is used to identify observations with intensities $> \psi$ as being atypical occurrences of episodic water releases. Note that as the threshold ψ increases, $E_{w,\psi}(i) \rightarrow 0$. Therefore, events that maintain $E_{w,\psi}(i) > 0$ at relatively high ψ can be considered as very unusual occurrences compared to the bulk of the NMS observations (abnormally high intensity events that occur with an abnormally high cadence).

Supplementary Fig. 17 presents the calculated normalized event intensity rate $E_{w,0}$. Instead of superimposing multiple curves that depict $E_{w,\psi}$ for other values of ψ, we chose to color each data point i in $E_{w,0}(i)$ according to the highest threshold value $\psi_{max}(i)$ for which $E_{w,\psi_{max}(i)}(i) > 0$. Peaks corresponding to atypical water release events are selected by an automatic algorithm based on the following two criteria:

$$\begin{cases} -\text{ The data point } i \text{ is a local maximum in } E_{w,0}, \\ -\text{ The maximum threshold of the data point } i\ is\ \psi_{max}(i) > \xi \times MAD \end{cases} \tag{42}$$

MAD being the Mean Absolute Deviation of all measurements (11.8 cm^{-3}), and ξ an adjustable factor that capture the degree of statistical significance of the peak. The higher ξ is, the more atypical and significant the event is. When combined, these two criteria isolate peaks that correspond to events with abnormally high magnitudes that occur with abnormally high cadences. We will refer to these events as "peak events". The timing and magnitudes of 45 identified peak events are marked in Supplementary Fig. 17 for the case of $\xi = 6$. A higher setting for ξ will yield fewer exceptional events, while a lower ξ will result in a much greater number. A $\xi = 6$ was found to generate the largest number of exceptional events with timings that correlate with established streams while minimizing the number of unidentified/uncorrelated events. The activities of most established meteor streams were observed to peak above the background for longer than a day. Therefore, we assume that any two identified exceptional events that are separated by less than a day belong to a single broader event. Additionally, a pair of peak events (identified as #7 in Supplementary Table 1) is consistent with the reported separate extrema for Comae Berenicids and are treated as a single stream. This results in the reduction of the identified number of exceptional events from 44 to 39.

References

47. Benna, M. *NMS PDS Software Interface Specification* (NASA's Planetary Atmospheres Node, 2014). [https://atmos.nmsu.edu/PDS/data/PDS4/LADEE/nms_bundle/document/nms_pds_sis.pdf].
48. Langmuir, I. The adsorption of gases on plane surfaces of glass, mica and platinum. *J. Am. Chem. Soc.* **40**, 1361–1403, doi:10.1021/ja02242a004 (1918).
49. Bird, G. A. *Molecular gas dynamics and the direct simulation of gas flows* (Oxford University Press, New York, 1994), pp. 80–84.
50. Mahaffy, P. R. *et al.* The Neutral Gas and Ion Mass Spectrometer on the Mars Atmosphere and Volatile Evolution Mission. *Space Sci. rev.* **195**, 49–73, doi: 10.1007/s11214-014-0091-1 (2015).
51. Norton, P. R., Tapping, R. L. & Goodale, J. W. A photoemission study of the interaction of Ni(100),(110) and (111) surfaces with oxygen. *Surf. Sci.* **65**, 13–36 (1977).
52. Hurley, D. H. Modeling of the vapor release from the LCROSS impact: I. Parametric dependencies. *J. Geophys. Lett.* **116**, E10007, doi:10.1029/2010JE003793 (2011).
53. Hurley, D. H. *et al.* Modeling of the vapor release from the LCROSS impact: II. Observations from LAMP. *J. Geophys. Lett.* **117**, E00H07, doi:10.1029/2011JE003841 (2012).
54. Hodges, R. R. Exospheric transport restrictions on water ice in lunar polar traps. *Geophys. Res. Lett.* **18**, 2113–2116, doi:10.1029/91GL02533 (1991).
55. Poston, M. J. *et al.* Temperature programmed desorption studies of water interactions with Apollo lunar samples 12001 and 72501. *Icarus* **255**, 24–29, doi:10.1016/j.icarus.2014.09.049 (2015).
56. Farrell, W. M., Hurley, D. M. & Zimmerman, M. I. Solar wind implantation into lunar regolith: Hydrogen retention in a surface with defects. *Icarus* **255**, 116–126, doi:10.1016/j.icarus.2014.09.014 (2015).
57. Farrell, W. M. *et al.* The statistical mechanics of solar wind hydroxylation at the Moon, within lunar magnetic anomalies, and at phobos. *J. Geophys. Res.* **122**, 269–389, doi:10.1002/2016JE005168 (2017).

58. Dohnanyi, J. S. On the origin and distribution of meteoroids. *J. Geophys. Res.* **75**, 3468–3493, doi:10.1029/JB075i017p03468 (1970).
59. Moussi, A., Drolshagen, G., McDonnell, J. A. M., Mandeville, J.C. & Kearsley, A. *in Proceedings of the 4th European Conference on Space Debris (ESA SP-587)*, 18–20 (2005).
60. Koschny, D. *et al.* Flux densities of meteoroids derived from optical double-station observations. *Planet. Space. Sci.* **143**, 230–237, doi:10.1016/j.pss.2016.12.007 (2017).
61. Morgan, T. H. & Killen, R. M. Production mechanisms for faint but possibly detectable coronae about asteroids. *Planet. Space. Sci.* **46**, 843–850, doi:10.1016/S0032-0633(98)00029-4 (1998).
62. Killen, R. M. Depletion of sulfur on the surface of asteroids and the moon. *Meteorit. Planet. Sci.* **38**, 383–388, doi: 10.1111/j.1945-5100.2003.tb00273.x (2003).
63. Lange, M. A & Ahrens, T. J. The evolution of an impact-generated atmosphere. *Icarus* **51**, 96–120, doi:10.1016/0019-1035(82)90031-8 (1982).
64. Ahrens, T. J. & O'Keefe, J. D. Equations of state and impact-induced shock-wave attenuation on the moon. *in Impact and Explosion Cratering* (Roddy, D. J. & Pepin, R. O. eds.), 639–656 (Pergamon Press , New York , 1977).
65. Holsapple, K. A. & Schmidt, R. M. Point source solutions and coupling parameters in cratering mechanics. *J. Geophys. Res.* **92**, 6350–6376, doi:10.1029/JB092iB07p06350 (1987).
66. Prieur, N. C. *et al.* The effect of target properties on transient crater scaling for simple craters, *J. Geophys. Res. Planets* **122**, 1704–1726, doi:10.1002/2017JE005283 (2017).
67. Collette, A. Sternovsky, Z. & Horanyi, M. Production of neutral gas by micrometeoroid impacts. *Icarus* **227**, 89–93, doi:10.1016/j.icarus.2013.09.009 (2014).
68. Stubbs, T. J. *et al.* The impact of meteoroid streams on the lunar atmosphere and dust environment during the LADEE mission, *45th Lunar Planet. Sci. Conf.*, LPI Contribution No. 1777, p. 2705 (2014).

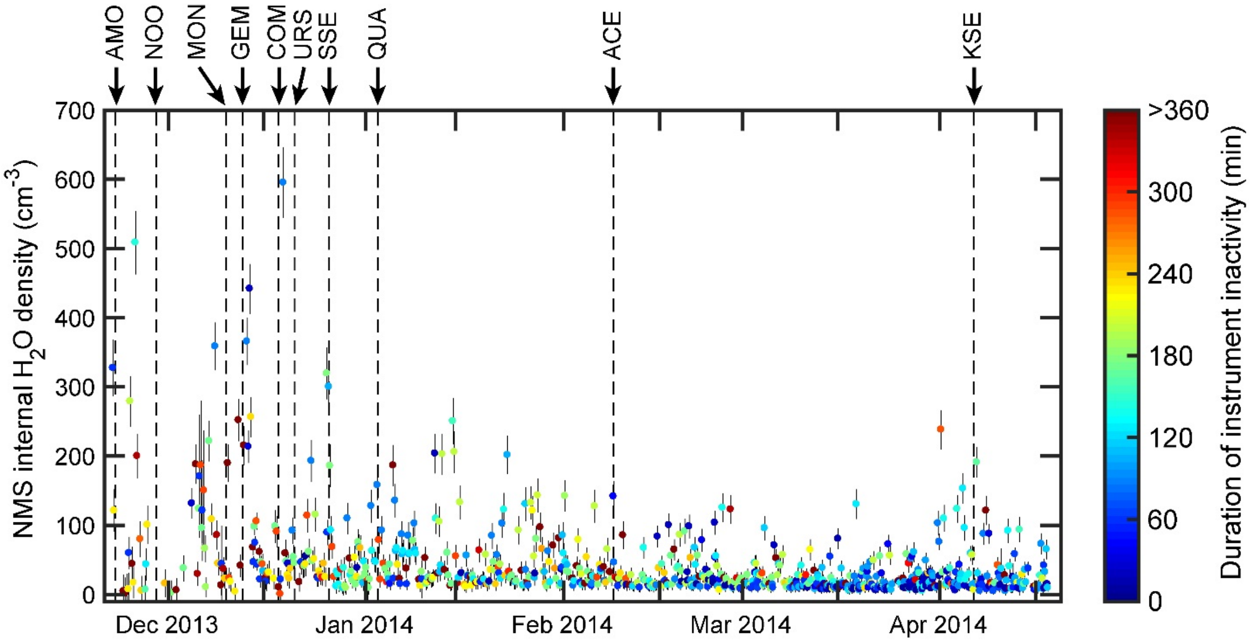

Supplementary Fig. 1 | Observed fluctuation of water background inside the NMS sensor. These measurements are reduced from data collected in the first few minutes of instrument turn-on. Each observation was collected following a period of inactivity (less than 360 min for 682 measurements). Error bars depicts 3σ levels of random errors. Water "events" are measurements that exhibit signals higher than the assessed 3σ level. Out of 743 measurements, 736 are considered to be water events. Standard deviations σ were assessed for these measurements and reflect uncertainties due to counting statistics and data processing. They are typically less than ±15% of the measured value. The measurements also bear a systematic error of ±30% (1σ) that is generated by the reduction scheme. Dashed lines mark the times of expected peaks of major meteoroid steams. The abbreviated designations for the streams are expanded in Supplementary Table 1.

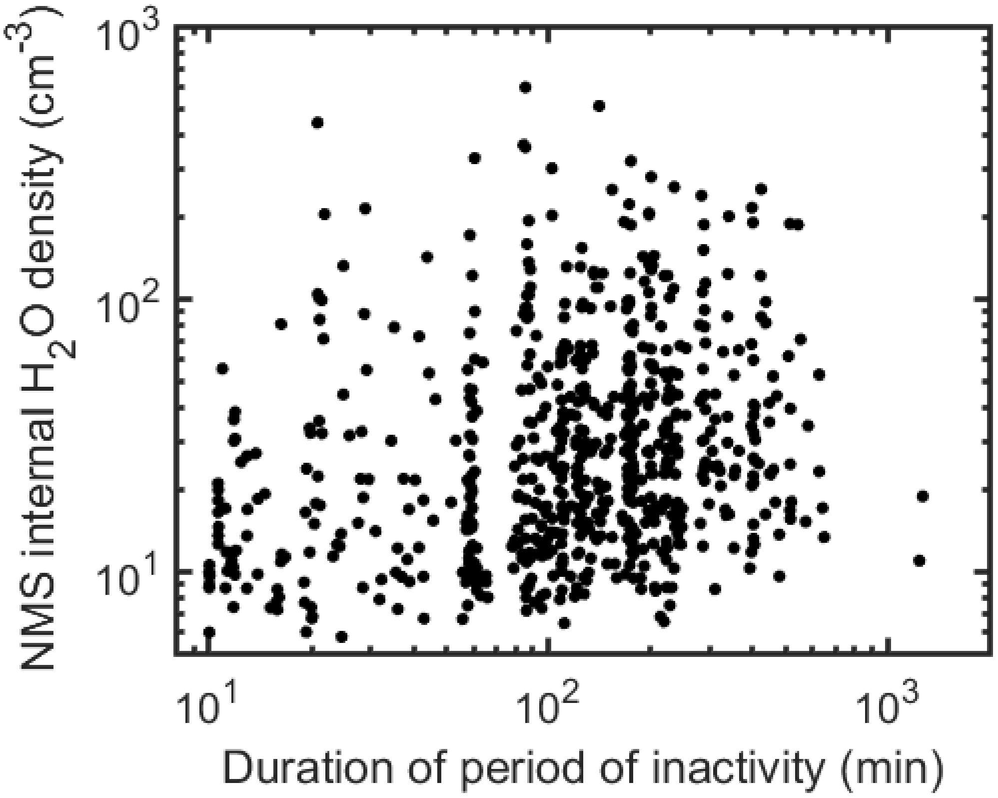

Supplementary Fig. 2 | Distribution of measured water densities as a function of the durations of period of the instrument's inactivity. This plot confirms the lack of strong correlation between the two.

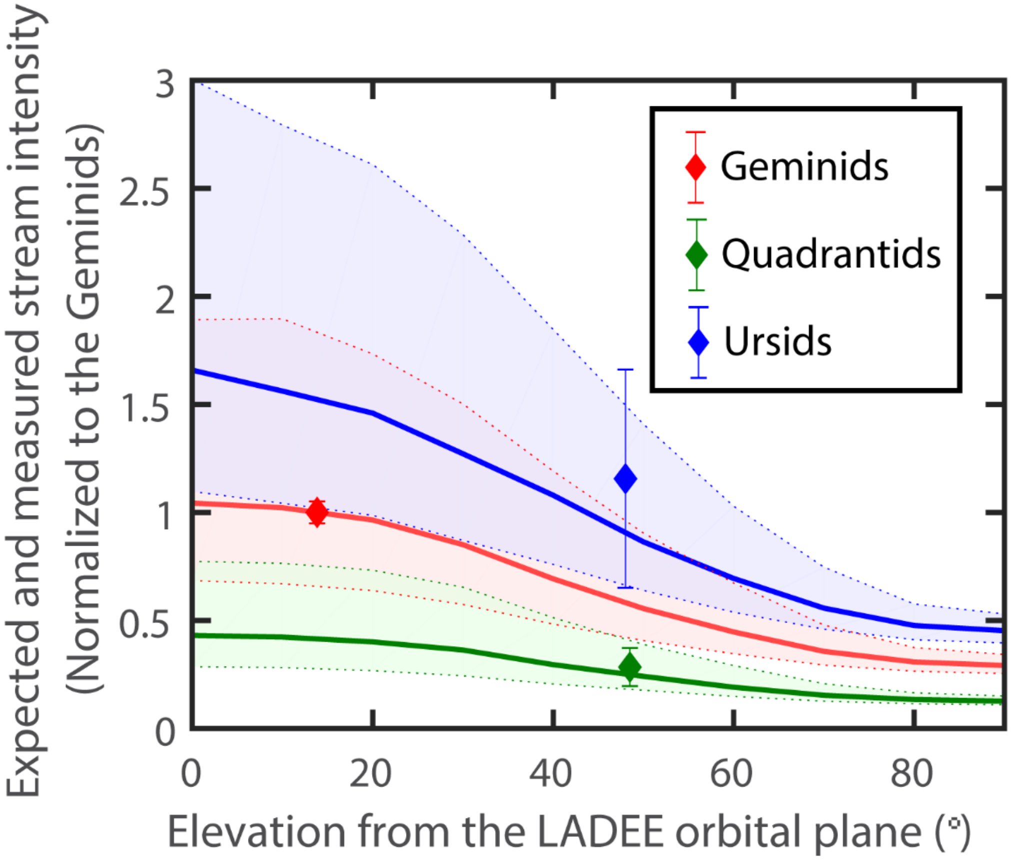

Supplementary Fig. 3 | Comparison between the expected and the NMS-measured event intensities. Solid lines depict the median event magnitudes of the expected NMS-observed events that would result from Geminid-, Ursid-, and Quadrantid-like streams for various radiant elevation with respect to the LADEE orbital plane. These profiles confirm NMS Moon-wide sensitivity to streams regardless of their radiant elevations. Event magnitudes are normalized by the Geminids NEIR/ZHR in order to provide a common base of comparison. Shaded areas reflect the 25-75 percentile range that are due to the stochastic variability of the observing start time and duration. The observed NEIR/ZHR for each stream is depicted by the colored diamonds bases on their respective elevations. Error bars reflect the 3σ uncertainties inherent to the IMO and NMS observations.

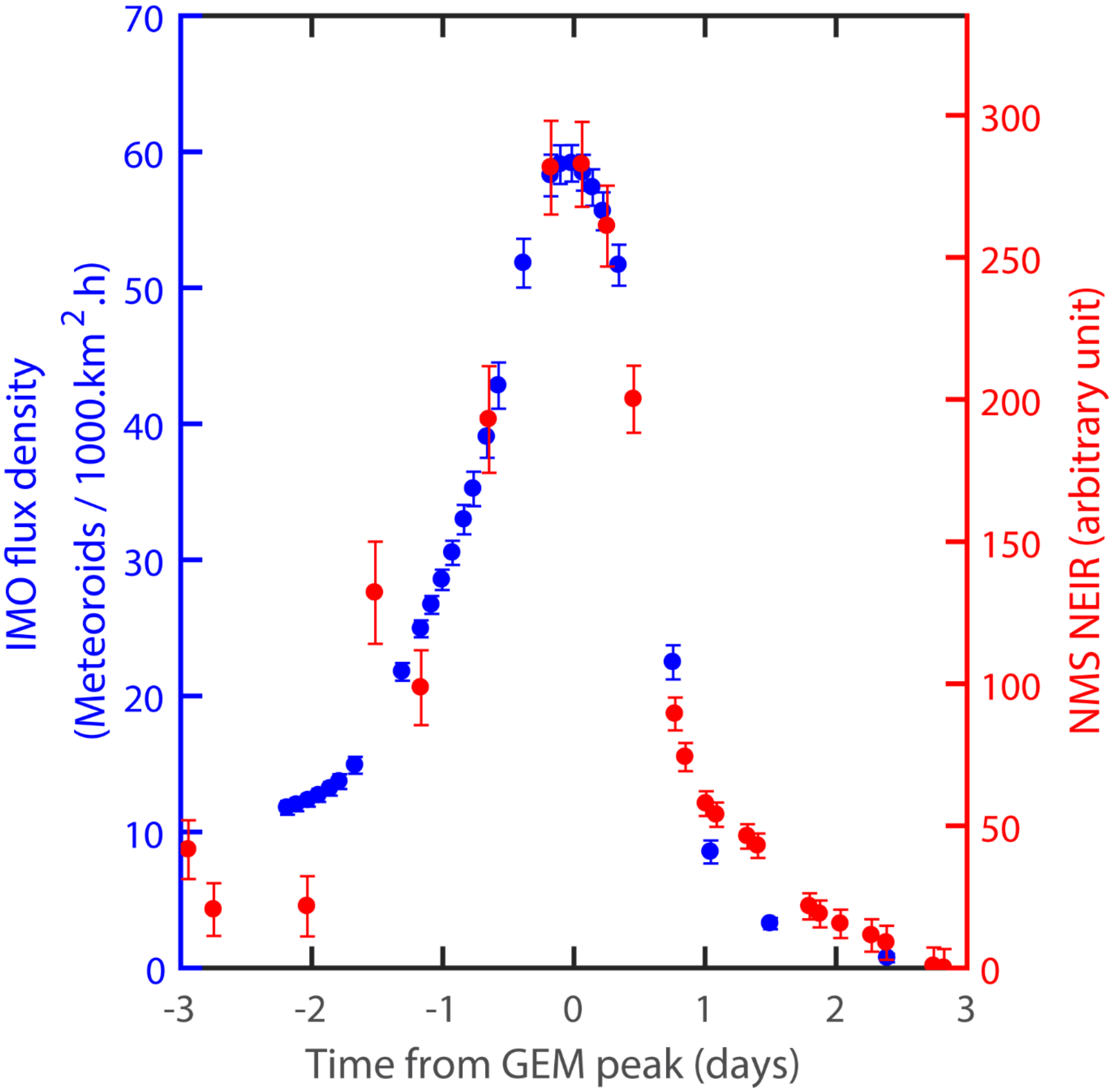

Supplementary Fig. 4 | Comparison between the IMO-reported flux density profile of the Geminids and the NMS-observed evolution of the NEIR. The IMO observations were collected by the IMO's Video Monitor Network[39] and were subjected to a Gaussian weighted averaging with a FWHM of 0.5 days (similar to that applied to the NMS data). Error bars reflect the 3σ uncertainties inherent to the IMO and NMS observations. A baseline NEIR=26.6 was subtracted from the NMS profile in order to extract the contribution of the Geminids from the background signal level.

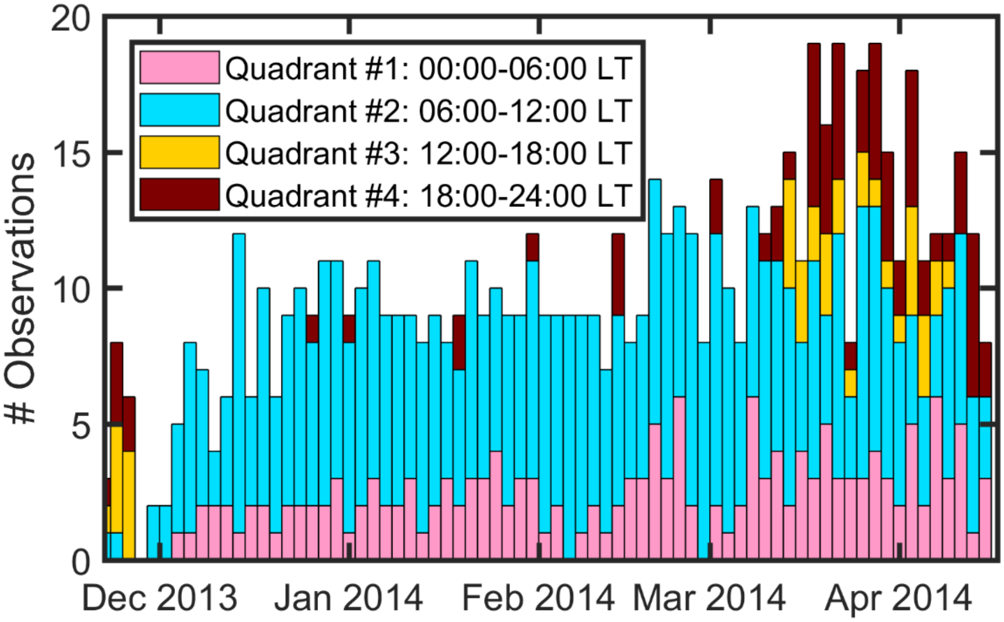

Supplementary Fig. 5 | Distribution of the number of NMS activities that collected water measurements over the duration of the science phase of the LADEE mission. The average observation rate over the duration of the mission is ~10/day. The local time quadrants pertain to the time of instrument turn-on. The water that is being measured was collected over the period of inactivity preceding the instrument's turn-on, which can extend over several orbits.

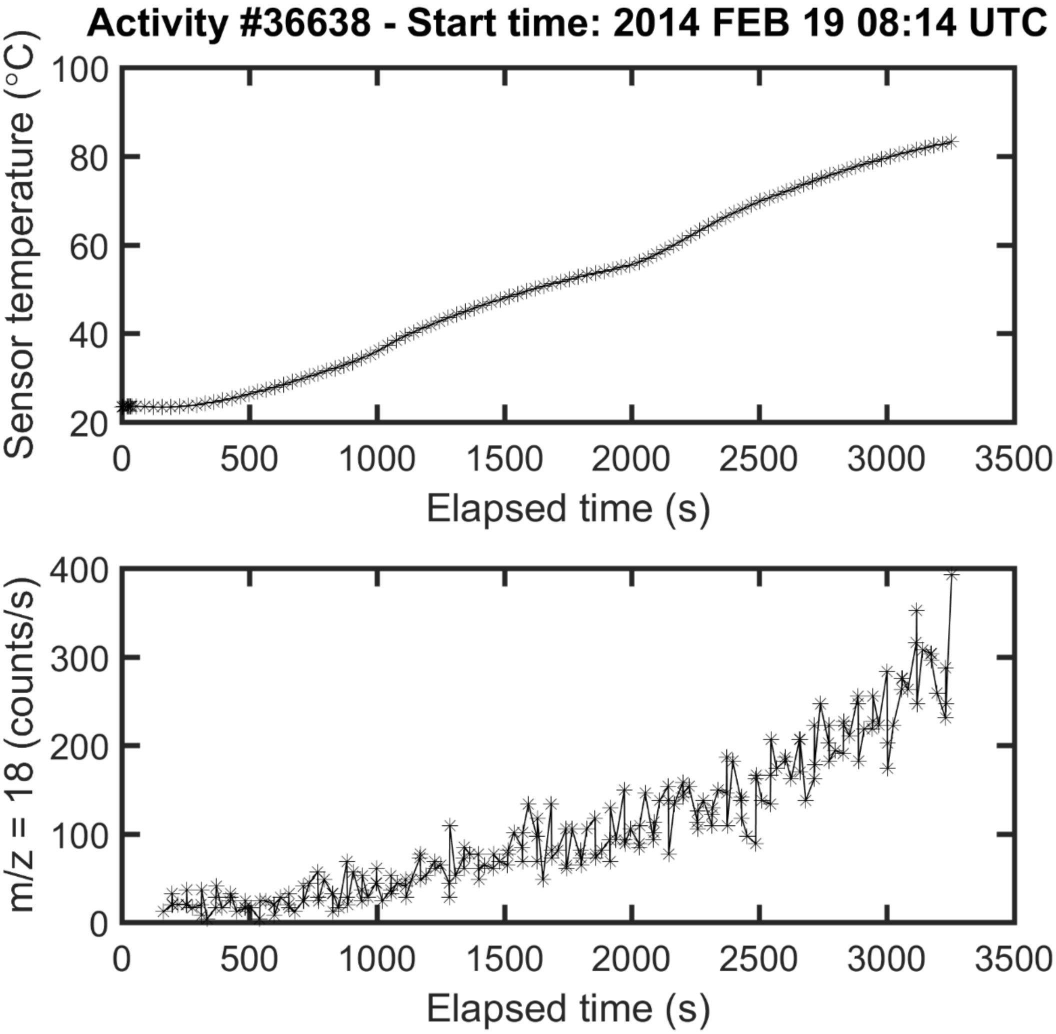

Supplementary Fig. 6 | Example of a typical signal profile measured during an NMS activity. Top plot: evolution of the sensor temperature over the course of the activity. The temperature is measured at the transfer tube leading to the ionization region, which is located ~4.5 cm from the filament emitter. **Bottom plot:** evolution of the count rate in the water channel. After the first few minutes of activity, the increase of outgassing from the warming instrument causes the signal to rise. Note that the water channel sampling starts after ~2 min from the beginning of the activity. These first 2 minutes are dedicated to the ramp-up of filament emission and the collection of engineering data on detector noise.

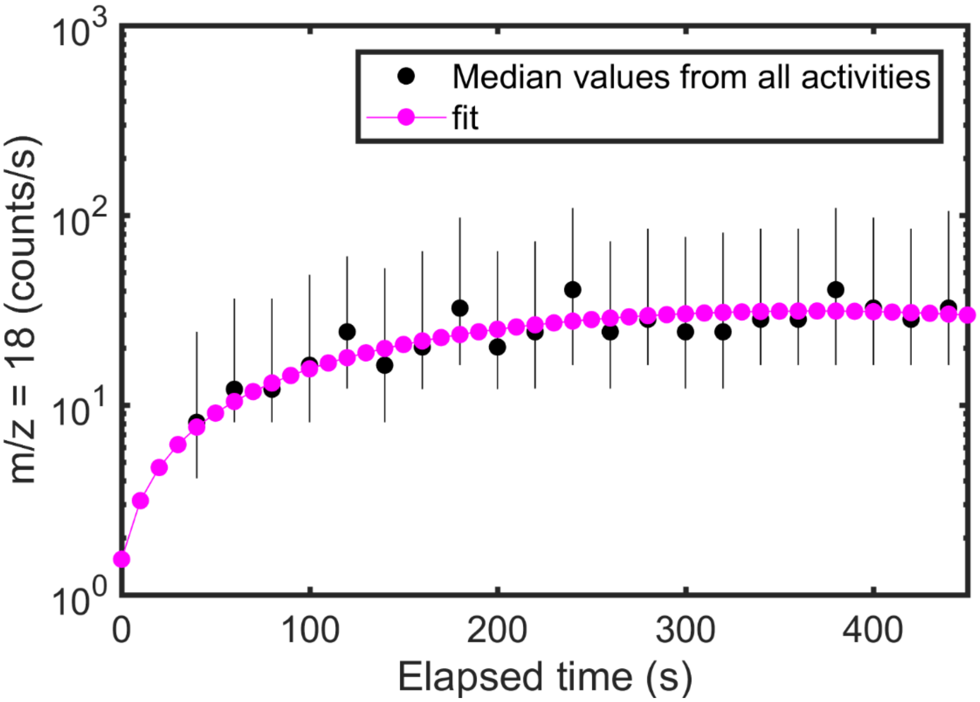

Supplementary Fig. 7 | Outgassing template (magenta) used to derive the amplitude of the water signal at the time of filament turn-on. This second-order polynomial function was derived from the median of binned amplitudes of all activities (black dots). The amplitude ranges depict the 25th and 75th percentiles on each time bin.

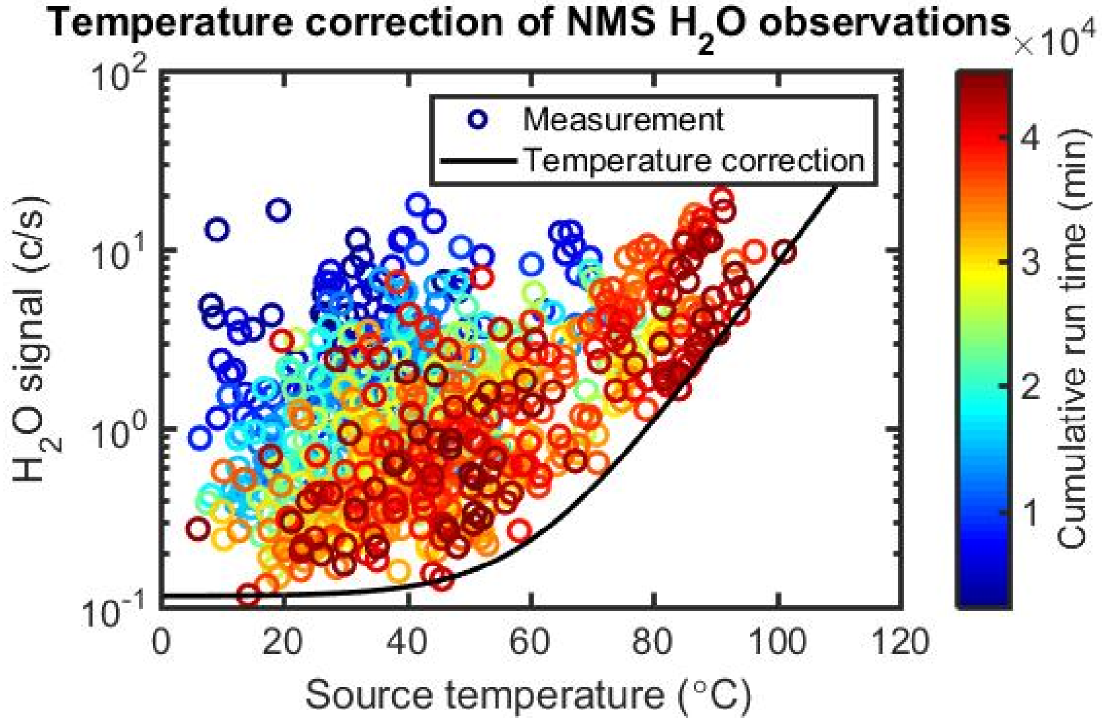

Supplementary Fig. 8 | Temperature correction of the raw water measurements. The temperature correction function (black line) is obtained by fitting the minima data points. Note that these minima data points were recorded in the second half of the mission when the intrinsic background of the instrument has reached its steady-state minimum.

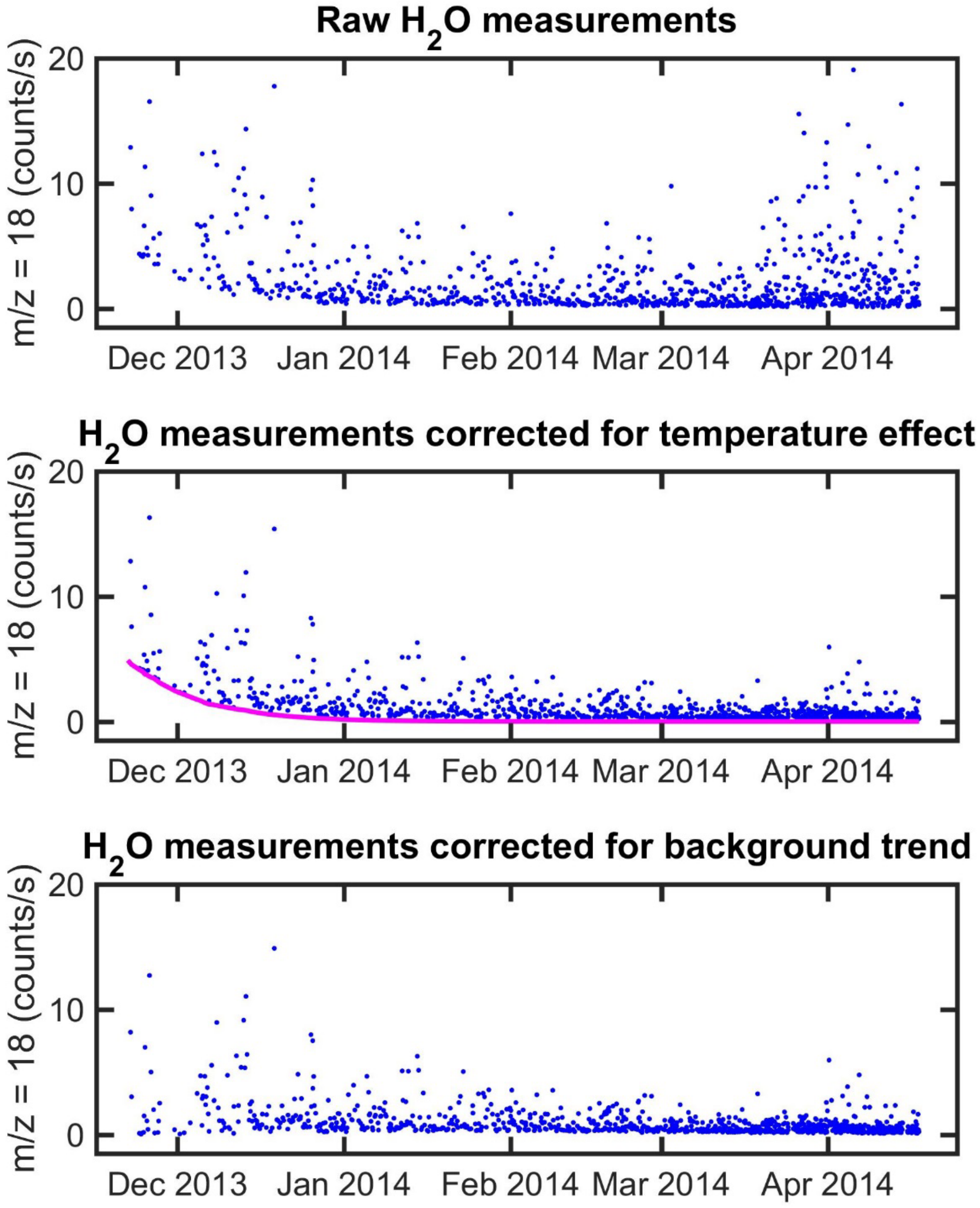
Raw H_2O measurements

H_2O measurements corrected for temperature effect

H_2O measurements corrected for background trend

Supplementary Fig. 9 | Summary plot depicting the processing steps that were applied to the water measurements. The raw water measurements at the time of instrument turn-on (top plot) were corrected for temperature (central plot). A fit of the intrinsic background was derived (magenta line) and subtracted from the temperature-corrected data.

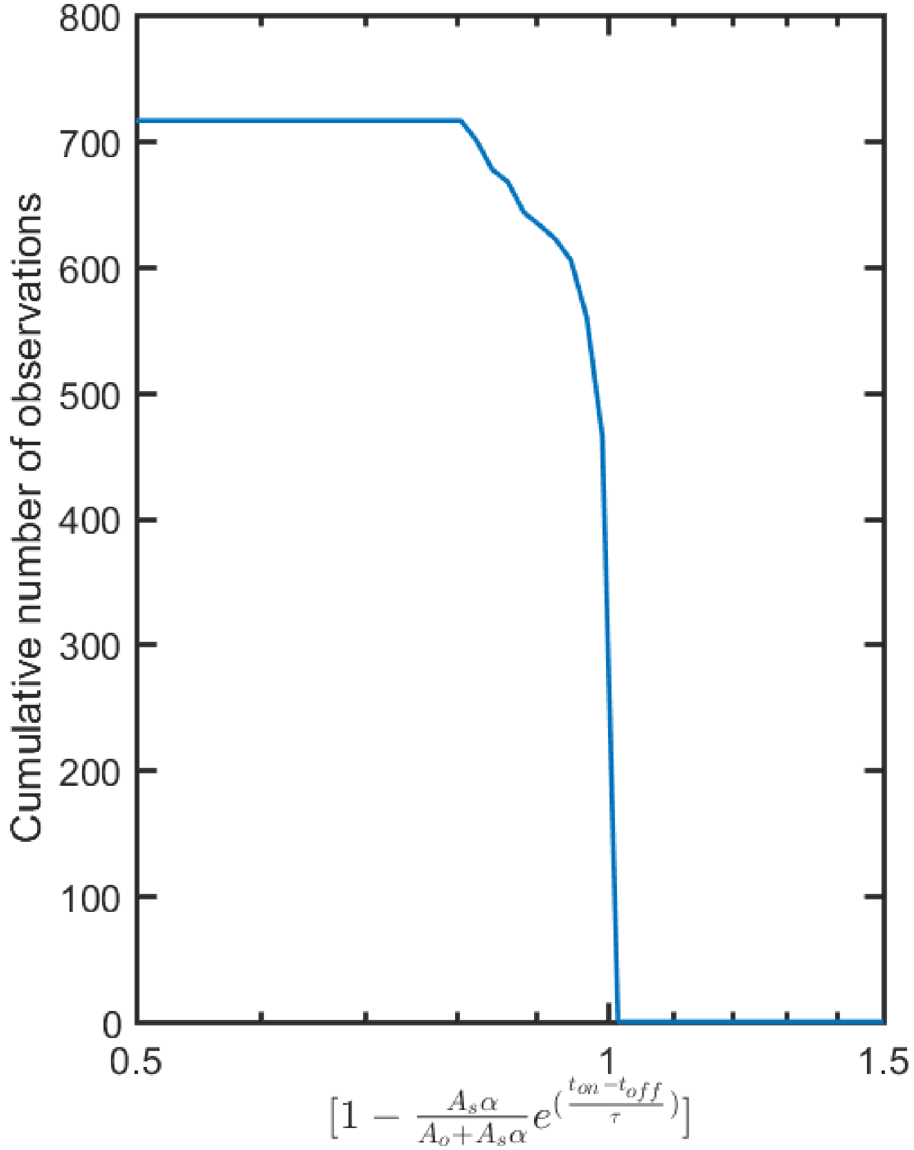

Supplementary Fig. 10 | Cumulative distribution function of observations as a function of the term $\left[1-\frac{A_s\alpha}{[A_o+A_s\alpha]}e^{-\frac{t_{on}-t_{off}}{\tau}}\right]$ in Eq. 23. The profile of this cumulative function is similar to the one derived for the case of a lunar surface lacking a desiccated layer (Fig. 2B).

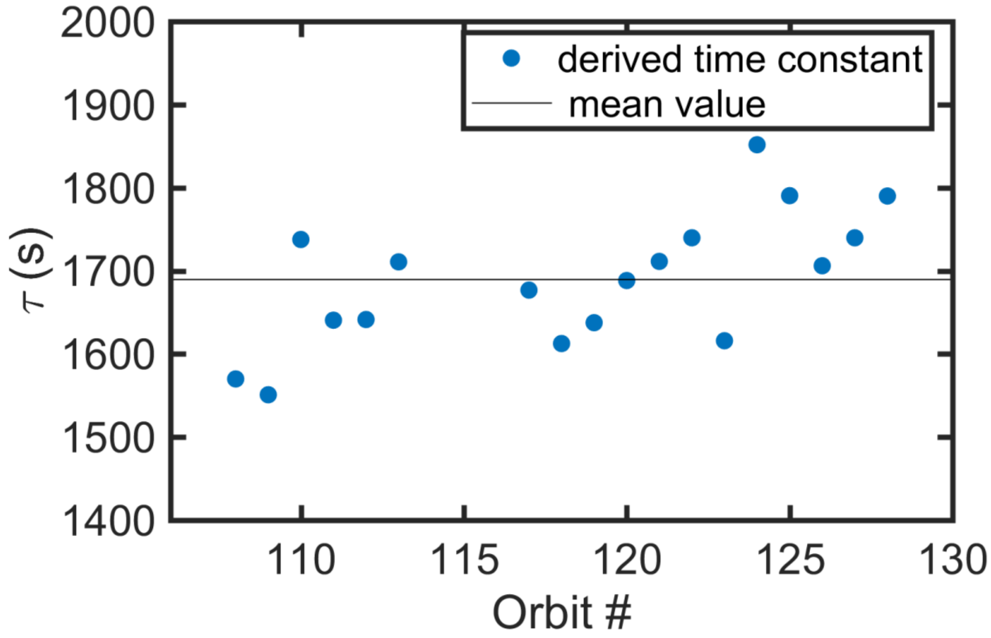

Supplementary Fig. 11 | Outgassing time constants derived from NGIMS data collected during 18 successive orbits (15-21 October 2014). These orbits are the first orbits after the instrument's initial exposure to the Martian atmosphere. The mean value is $\tau = 1689\text{s} \pm 79\text{s}$. The uncertainty is calculated as a standard deviation of the derived values.

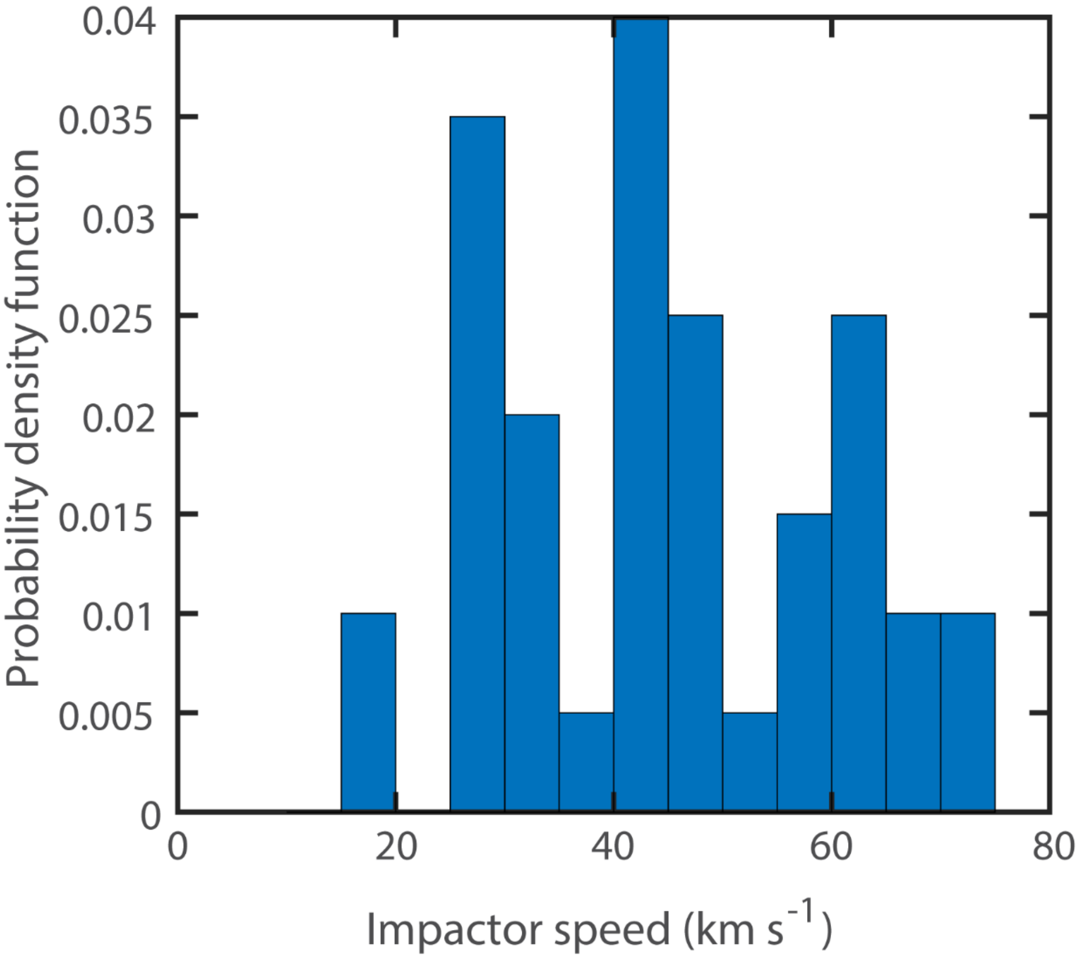

Supplementary Fig. 12 | Probability density function of impactor velocity. This probability density function mimics the speed distribution of the streams that encountered the Moon during the science phase of the LADEE mission (Supplementary Table 1).

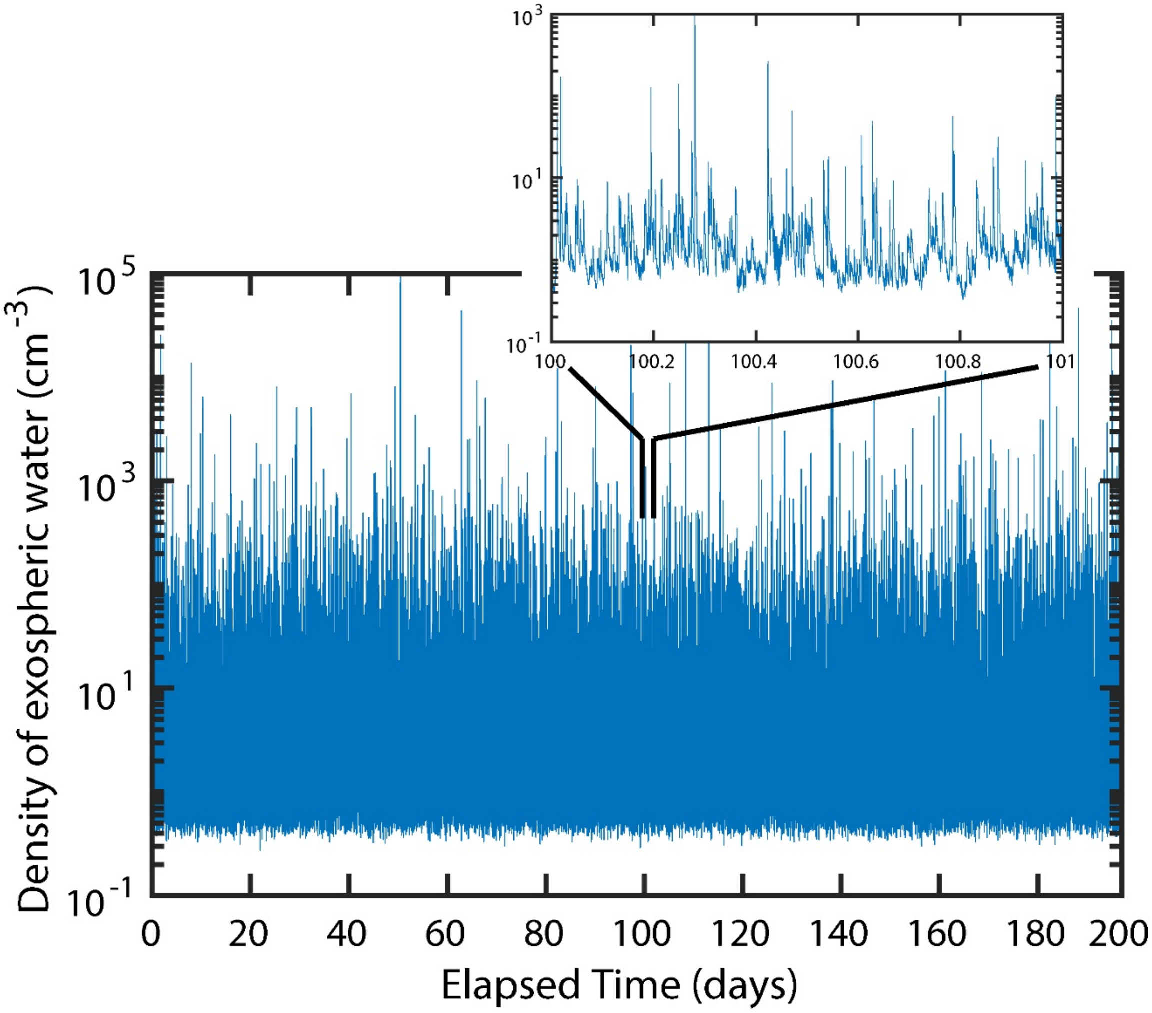

Supplementary Fig. 13 | Example of along-the-track water density that would be encountered by the LADEE spacecraft as it orbited the Moon. This density profile was constructed by accounting for the individual contribution of more than 2×10^{15} randomly generated impactors with masses ranging between 10^{-12} g and 10^{6} g. Water mass fluxes were calculated for the best fit case (Fig. 2) of lunar surfaces with 8.0 cm desiccated layer on top of 520 ppm hydrated soils (T_e= 5000 K).

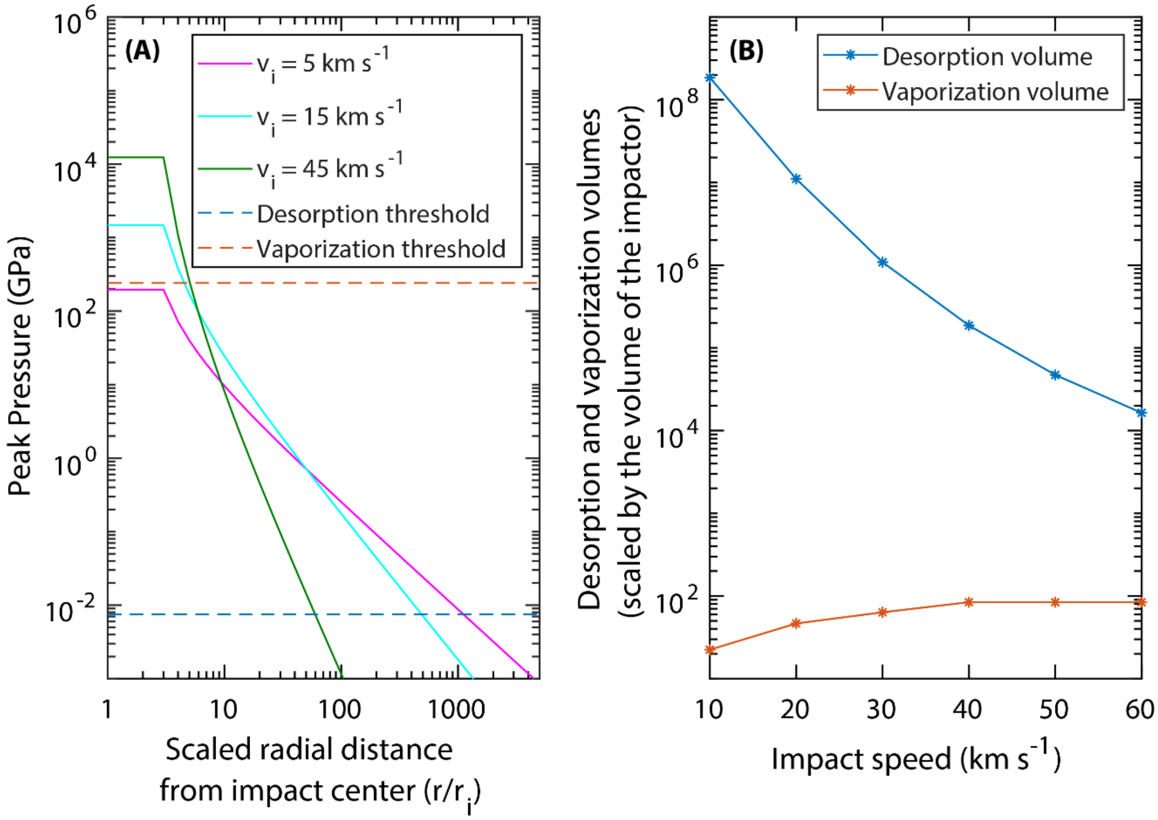

Supplementary Fig. 14 | Modeled decay of peak pressure as a function of radial distance for impacts into a regolith target at speeds of 5, 15, and 45 km s^{-1}. (A) The computed rate of pressure decline in the far field region ranges between $1/r^{1/3}$ for the lowest speed to $1/r^3$ for the highest speed. These decay trends are comparable to those provided by Ahrens and O'Keefe[64] for impact into anorthite. The volumes of regolith undergoing complete vaporization and desorption are estimated using a vaporization threshold of 236 GPa[43], and a desorption threshold of 7.8 MPa (derived from Eq. 36 assuming a hydration $H = 520$ ppm. **(B)** The velocity-dependent pressure decay law generates an increasing vaporization volume with increasing impact speed (as $\sim v_i$). However, it yields a decreasing desorption volume with increasing impact speed.

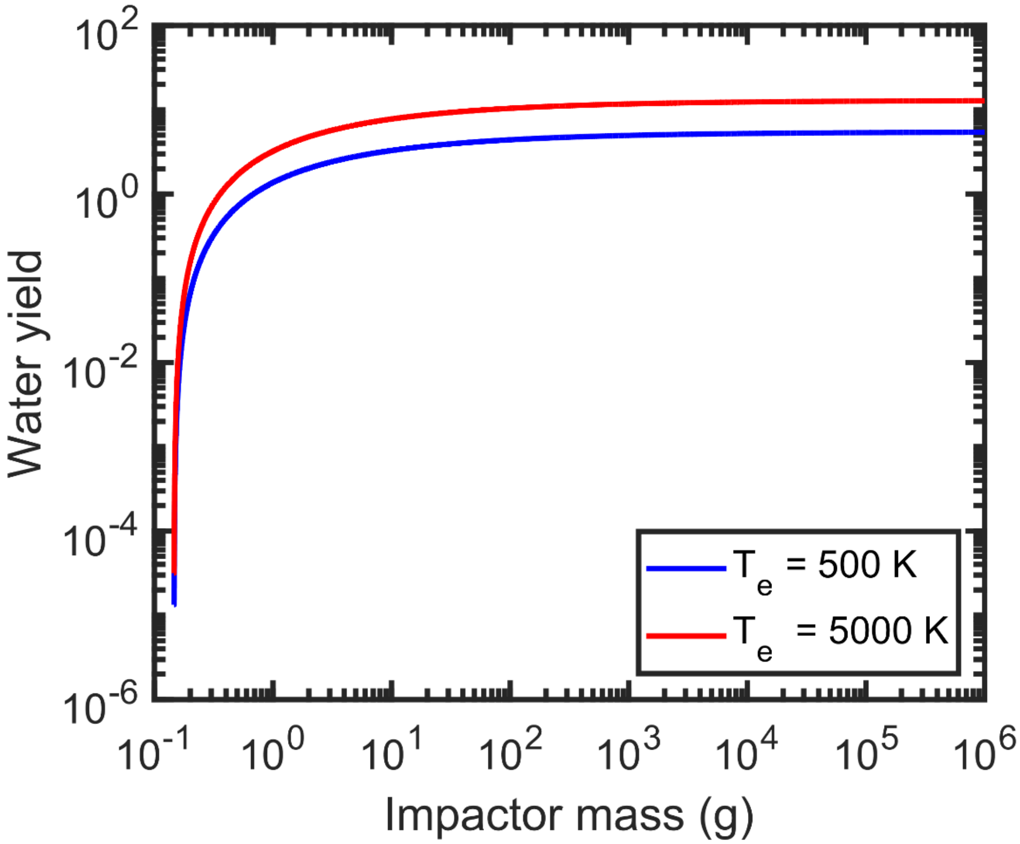

Supplementary Fig. 15 | Derived water yield as a function of impactor mass on a regolith surface. These curves were calculated assuming an 8 cm desiccated top layer for the two extreme cases of exospheric temperatures. For large impactors, the yield converges asymptotically to 5.4 for T_e = 500 K, and 12.8 for T_e = 5000 K. Impacts with masses less than 0.15 g are not large enough to break through the dry layer. Consequently, they yield no water.

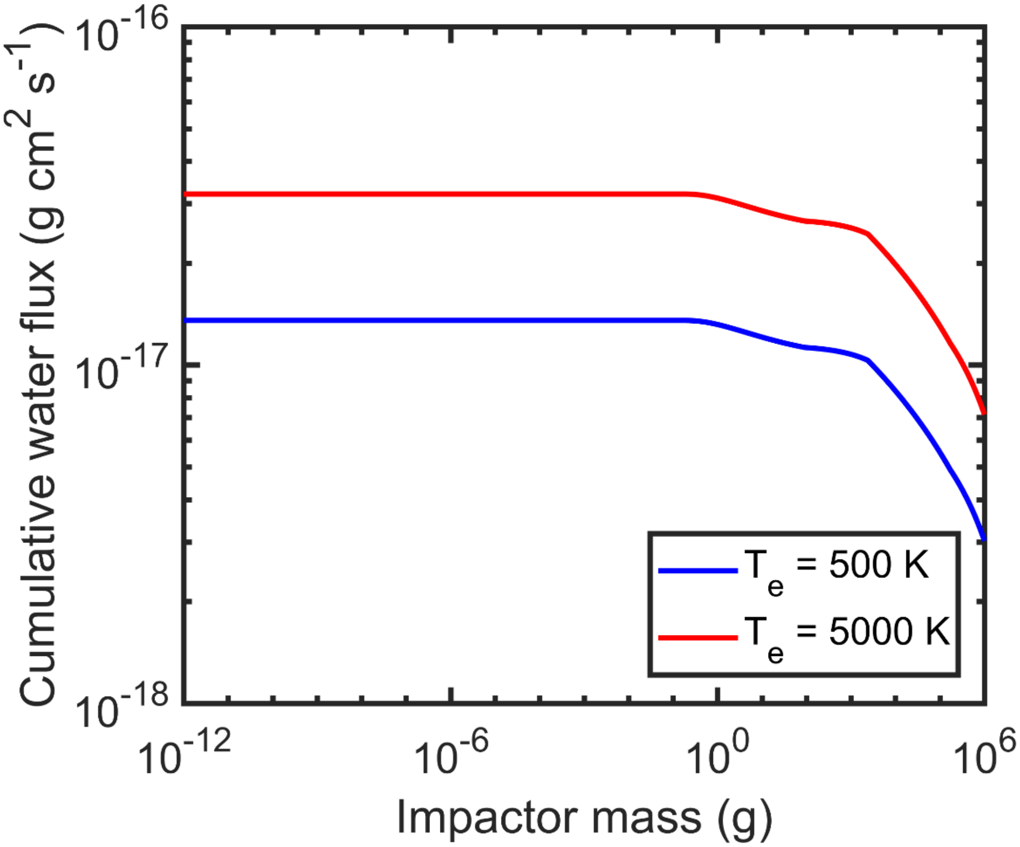

Supplementary Fig. 16 | Derived water loss rate as function of impactor mass for the case of exospheric temperatures *T_e* = 500 K, and *T_e* = 5000 K. The total loss rate due to all meteoroid impacts is 1.3×10^{-17} g cm^2 s^{-1}, and 3.2×10^{-17} g cm^2 s^{-1}, respectively. Impacts with masses less than 0.15 g are not large enough to break through the desiccated layer and, as such, do not contribute to the total water loss.

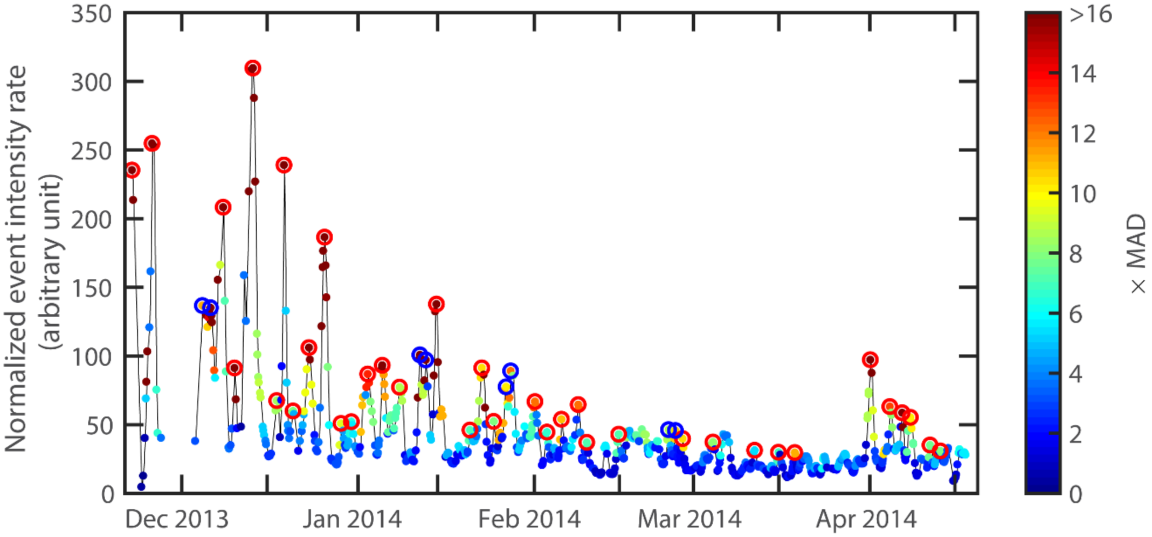

Supplementary Fig. 17 | Calculated normalized event intensity rate for a signal threshold $\boldsymbol{\psi = 0}$ ($\boldsymbol{E_{w,0}}$). Each data point i is color coded according to $\psi_{max}(i)$ for which $E_{w,\psi_{max}(i)}(i) > 0$. An automatic picking algorithm identified 44 exceptional events as peaks with $\psi_{max}(i) > 6 \times MAD$ (data points encircled in red or blue). Of these, 4 pairs of events (data points encircled in blue) were separated by less than a day, which are considered as the signature of a broader but a single event.

Stream	IAU #	Code	ZHR	V_g	Predicted Peak	Observed Peak	ΔT	ID	Notes
Leonids	**013**	**LEO**	**15**	**72.5**	**17-Nov-2013 07:14**	23-Nov-2013 12:00	-	1	First NMS measurement. Does not capture the stream peak
alpha Monocerotids	246	AMO	Var	63.0	21-Nov-2013 06:15				
November theta Aurigids	390	THA		32.5	26-Nov-2013 03:46	26-Nov-2013 21:36	-17.8	2	
November Orionids	**250**	**NOO**		**-**	**29-Nov-2013 07:16**	-	-	A	Instrument not operating
December kappa Draconids	336	DKD		-	03-Dec-2013 07:45	-	-	B	Instrument not operating
Southern chi Orionids	**257**	**ORS**		**-**	**03-Dec-2013 16:25**				
December phi Cassiopeiids	446	DPC		-	04-Dec-2013 05:46				
psi Ursae Majorids	339	PSU		61.7	05-Dec-2013 03:42	05-Dec-2013 16:48	-10.6	3	Two NMS peaks separated by 0.9 day
Phoenicids	**254**	**PHO**	**Var**	**18.0**	**05-Dec-2013 06:08**				
December alpha Draconids	**334**	**DAD**		**40.8**	**08-Dec-2013 12:30**	08-Dec-2013 21:36	-9.6	4	
eta Hydrids	529	EHY		62.5	09-Dec-2013 05:10				
sigma Hydrids	016	HYD	3	58.9	11-Dec-2013 13:22	11-Dec-2013 19:12	15.9	5	
December Monocerotids	**019**	**MON**	**2**	**41.4**	**12-Dec-2013 11:04**				
Geminids	**004**	**GEM**	**120**	**33.8**	**13-Dec-2013 17:55**	14-Dec-2013 12:00	-18.1	6	
December sigma Virginids	428	DSV		66.2	14-Dec-2013 03:10				
December chi Virginids	335	XVI		69.1	13-Dec-2013 22:36				
Comae Berenicids	020	COM	3	63.3	19-Dec-2013 19:42	20-Dec-2013 02:24	-6.7	7	Two separate extrema reported by (42), and (43)
Ursids	015	URS	10	32.9	22-Dec-2013 12:27	21-Dec-2013 19:12	17.2	8	
alpha Lyncids	252	ALY		49.5	23-Dec-2013 17:32	24-Dec-2013 12:00	-18.5	9	
sigma Serpentids	330	SSE		45.5	26-Dec-2013 22:09	27-Dec-2013 04:48	-6.6	10	
alpha Hydrids	331	AHY		43.3	30-Dec-2013 16:22	30-Dec-2013 07:12	9.2	11	
alpha Hydrids	331	AHY		43.3	31-Dec-2013 16:41	31-Dec-2013 21:36	-4.9	12	

Supplementary Table 1 | Continues on next page

Stream	IAU #	Code	ZHR	V_g	Predicted Peak	Observed Peak	ΔT	ID	Notes
January Leonids	319	JLE		**51.4**	02-Jan-2014 08:14	03-Jan-2014 19:12	3.2	13	Shoulder of Quadrantids
Quadrantids	**010**	**QUA**	**120**	**40.3**	**03-Jan-2014 22:22**				
alpha Hydrids	331	AHY		43.3	04-Jan-2014 14:31				Shoulder of Quadrantids
alpha Hydrids	331	AHY		43.3	06-Jan-2014 11:48	06-Jan-2014 09:36	2.2	14	
Unidentified		NEW				09-Jan-2014 09:36		15	Possibly a new stream
Northern delta Cancrids	96	NCC		27.2	13-Jan-2014 10:53	13-Jan-2014 12:00	-1.1	16	Two NMS peaks separated by 1.0 day
Bootid-Coronae Borealid	**332**	**BCB**		**43.0**	**15-Jan-2014 22:32**	15-Jan-2014 21:36	0.9	17	BCB complex includes 321/TCB, 322/LBO, and 323/XCB. Seen as a broad peak (2.5 days) by NMS
Northern delta Cancrids	96	NCC		27.2	17-Jan-2014 00:00				
Southern delta Cancrids	97	SCC		27.0	17-Jan-2014 08:56				
January xi Ursae Majorids	341	XUM		45.6	18-Jan-2014 14:46	-	-	C	Undetected
gamma Ursae Minorids	404	GUM		28.8	19-Jan-2014 18:24	21-Jan-2014 19:12	-48.7	18	
eta Corvids	530	ECV		70.3	23-Jan-2014 03:49	23-Jan-2014 21:36	-17.8	19	
Daytime xi Sagittariids	100	XSA		26.3	25-Jan-2014 00:42	26-Jan-2014 00:00	-23.3	20	
omicron Hydrids	569	OHY		59.1	30-Jan-2014 16:08	29-Jan-2014 09:36	30.5	21	Two NMS peaks separated by 0.8 day
alpha Antliids	110	AAN		45.0	02-Feb-2014 18:00	02-Feb-2014 04:48	13.2	22	
February epsilon Virginids	**506**	**FEV**		**62.9**	**04-Feb-2014 05:37**	04-Feb-2014 07:12	-1.6	23	
February eta Draconids	424	FED			04-Feb-2014 06:56				
Unidentified		UNI				06-Feb-2014 21:36		24	Possibly: February alpha Orionids (270/FAO)
alpha Centaurids	102	ACE	6	56.0	08-Feb-2014 21:29	09-Feb-2014 19:12	-21.7	25	
Unidentified		UNI				11-Feb-2014 07:12		26	Several possible faint streams
Unidentified		UNI				17-Feb-2014 00:00		27	Several possible faint streams
Unidentified		UNI				26-Feb-2014 07:12		28	Two NMS peaks separated by 0.9 day Possibly: February γ Virginids (732/FGV)
Unidentified		UNI				28-Feb-2014 04:48		29	Possibly: η Draconids (906/ETD)
Unidentified		UNI				05-Mar-2014 12:00		30	Possibly: March 12 Bootids (859/MTB)

Supplementary Table 1 | Continues on next page

Stream	IAU #	Code	ZHR	V_g	Predicted Peak	Observed Peak	ΔT	ID	Notes
x Herculids	346	XHE		35.2	12-Mar-2014 23:17	12-Mar-2014 21:36	1.7	31	
eta Virginids	11	EVI		26.6	17-Mar-2014 20:27	17-Mar-2014 02:24	18.0	32	
Daytime kappa Aquariids	128	MKA		33.2	20-Mar-2014 11:58	19-Mar-2014 21:36	14.4	33	
Unidentified		NEW				02-Apr-2014 04:48		34	Possibly a new stream
Unidentified		NEW				05-Apr-2014 14:24		35	Possibly a new stream
kappa Serpentids	27	KSE		46.7	07-Apr-2014 07:12	07-Apr-2014 19:12	-12.0	36	
Unidentified		NEW				09-Apr-2014 07:12		37	Possibly a new stream
Alpha Virginids	21	AVB		17.6	11-Apr-2014 23:33	12-Apr-2014 16:48	-17.5	38	
Daytime April Piscids	144	APS		29.2	14-Apr-2014 18:14	14-Apr-2014 12:00	6.2	39	

Supplementary Table 1 | List of established meteor streams that should have been encountered by the Earth-Moon system during the course of the LADEE science phase and their correlation with the NMS observations (Also shown in Fig. 1). The table also lists streams that were detected by NMS but do not have a matching candidate in the IAU established list. Columns are: Stream name; IAU number; IAU meteor shower code; ZHR= expected Zenithal Hourly Rate (hr^{-1}) when known[28], V_g = is the geocentric speed of the stream ($km\ s^{-1}$); Predicted stream peak time (UT); Observed NMS peak time (UT) derived from the normalized event intensity rate of the NMS observations; ΔT = Predicted time-Observed time (hours); ID = stream identification in Fig. 1; and Notes. The list of established streams is compiled and maintained by the IAU Meteor Data Center (MDC)[25,28]. When several streams are coincident in time, the major stream is highlighted in bold. Of the 32 established meteor stream groups, 29 were detected as spikes in the NMS-derived event intensity rate, 2 stream groups occurred over a period during which the instrument was not operating, and 1 stream was not detected. Additionally, 10 signatures labeled “Unidentified” could not be attributed to any streams from the established list. In 6 cases, a possible match based on the peak time and intensity could be found in the MDC working list. The names of the possible stream candidates are provided in the Note column. The remaining 4 represent the discovery of new streams since they do not correspond to any previously established streams, and their signatures are too strong and well-defined to potentially match one of the weak streams reported in the MDC’s working list.

Stream	V_m (km s^{-1})	Lat $_{SSE}$ (°)	LT $_{SSE}$ (hh:mm)	θ (°)	IMO Observed Peak ZHR Intensity (hr^{-1})	NMS Observed Peak NEIR (arb. unit)	Observed Normalized NEIR/ZHR	Expected Normalized NEIR/ZHR (median)
Geminids	35.5	+10.21	01:56	+13.84	133±8	309.2±14.9	1.00±0.08	1.00
Ursids	32.9	+72.62	02:58	+48.01	22±9	59.6±9.1	1.16±0.51	0.91
Quadrantids	41.0	+64.82	06:23	+48.52	130±38	86.5±8.9	0.28±0.09	0.25

Supplementary Table 2 | Parameters used in the comparison of the magnitudes of the peak events of the Geminids, Ursids, and Quadrantids. V_m is the selenocentric speed of the stream. Lat_{SSE} and LT_{SSE} are the latitude and local time of the stream normal in selenocentric Solar Ecliptic (SSE) coordinates. θ is the elevation of the stream's radiant with respect of the LADEE orbital plane (calculated at the time of the stream peak activity)[68]. The ZHRs are based on what was reported on by the IMO[28] in 2013 – 2014.